DEFORMATION HETEROGENEITY IN TEXTURED MAGNESIUM AZ31 UNDER REVERSED LOADING

by

Enver Kapan

B.S., Mechanical Engineering, Boğaziçi University, 2013

Submitted to the Institute for Graduate Studies in
Science and Engineering in partial fulfillment of
the requirements for the degree of
Master of Science

Graduate Program in Mechanical Engineering
Boğaziçi University

2016

DEFORMATION HETEROGENEITY IN TEXTURED MAGNESIUM AZ31 UNDER REVERSED LOADING

APPROVED BY:

Assoc. Prof. Can Aydıner (Thesis Supervisor)	.....
Assist. Prof. Jeremy Kyle Mason	.....
Assist. Prof. Alpay Oral	.....

DATE OF APPROVAL: 25.07.2016

ACKNOWLEDGEMENTS

I would like to thank to my parents for their endless support for me. My dad, İsmail Kapan has always inspired me with his unending passion for knowledge although our fields of study are quite different. He always encouraged me to continue with the intellectual career that I have been dreaming for since my childhood. My mom, Sevim Kapan, probably the reason for me to be the person that I am now, literally suffered a lot while raising up me. Yet I have not seen a day that she was weary of this. I cannot repay, in any way, for what they have done for me and they already know that.

I am deeply grateful to Assoc. Prof. Can Aydıner for all the guidance, advisory support and friendship that he generously offered. He, not just as a thesis advisor but also as a close friend, got me back on my legs when I tend to fall during the exhausting course of this experimental research. I learned a lot from him. He taught me nearly all the knowledge that I know about experimental science and the value of it.

I would like to thank to Assist. Prof. Jeremy Mason and Assist. Prof. Alpay Oral for their invaluable suggestions about my study. In fact, thanks to their discussions, I was able to rectify some of the critical remarks I made in the text. Prof. Jeremy Mason read the each and every word of the first draft this thesis and pointed out even the simplest mistakes I have done. They both contributed greatly to the intellectual aspects of the thesis.

I want to thank all the folks of the Mechanical Engineering department. In particular, my lab mates Nima Shafaghi, Sevinç Uçar and Olcay Türkoğlu have put a great deal of physical and intellectual effort especially during the unending days of experiments. I have learnt a lot from Kenan Çınar who was like a master to me in the first year of my study. Mustafa Şengör and Buğra Üçel have been great companies to me.

This work was in part supported by the Scientific and Technological Research Council of Turkey (TÜBİTAK), Grant No: 114M215.

ABSTRACT

DEFORMATION HETEROGENEITY IN TEXTURED MAGNESIUM AZ31 UNDER REVERSED LOADING

The evolution of heterogeneous deformation fields in rolled Mg AZ31 under compression -tension-compression loading along the rolling direction is investigated with multiscale digital image correlation. Full-field deformation maps with sub-grain resolution are obtained at each analysis point. Heterogeneous shear bands are found to govern the deformation behavior through all stages of loading. On the compressive loading stages, $\pm 45^{\circ}$ shear bands, generated by collaborative activity of $\{10\bar{1}2\}\langle\bar{1}011\rangle$ tensile twin mechanism, dominate the plastic behavior. At all length scales, these bands are observed to have an abrupt and sudden nature in agreement with the abrupt and sudden nature of deformation twinning. Besides, these shear bands are concluded to be the products of macroscale and microscale simple shear processes. Upon reversal of loading, $\pm 45^{\circ}$ shear bands are recovered in a reversible fashion due to detwinning. Further tensile loading after the detwinning mechanism has finished lead to the formation of very localized and intense shear bands that appear slanted at approximately 60°. On the second compression stage, new $\pm 45^{\circ}$ shear bands form and intermingle with the preexisting high angle shear bands. A possible mechanism for cyclic hardening in Mg AZ31 materials due to this intermingling effect is discussed. Volumetric information is deduced by inspection of an orthogonal face to the primary observation face of the sample with another set of DIC optics. Volumetric information confirms volumetric nature of $\pm 45^{\circ}$ simple shear processes that form during compression stages. For the tensile stages, macro-DIC analysis of primary and secondary surfaces and micro-DIC analysis of the primary surface point to change of dominant deformation mechanisms during different loading stages.

ÖZET

TEKSTÜRLÜ MAGNEZYUM ALAŞIMININ TERS YÜKLEME ALTINDA HETEROJEN DEFORMASYONU

Haddelenmiş Mg AZ malzemesinde, hadde yönünde basma-çekme-basma yüklemesi esnasında oluşan heterojen gerinim alanları dijital imge korelasyonu metodu ile, makroskopik ve mikroskopik ölçeklerde incelenmiştir. Tam saha gerinim haritaları tanecik boyutu ölçeğinde elde edilmiştir. Bütün yükleme evrelerinde heterojen kesme bantlarının deformasyon davranı- şını belirlediği saptanmıştır. Basma yüklemesi sırasında, $\{10\bar{1}2\}\langle\bar{1}011\rangle$ ikizlenme mekanizmalarının aktivitesi neticesinde oluşan $\pm 45^{\circ}$ kesme bantları malzemenin plastik davranışını belirleyici olmuştur. Bütün ölçeklerde bu bantların ani şekilde oluştuğu ikizlenme mekanizmasının ani ve ansız tabiatine uygun şekilde gözlemlenmiştir. Ayrıca, bu kesme bantlarının bütün ölçeklerde basit kesme hareketlerinin bir neticesi olduğu teslim edilmiştir. Yükleme yönünün tersine çevrilmesiyle, daha önce oluşmuş olan $\pm 45^{\circ}$ kesme bantları geri-ikizlenme mekanizması ile geri dönmüştür. Çekme yüklemesine devam etme neticesinde lokalize ve yoğun plaka normaline yaklaşık 60° eğimde olan kesme bantlarının oluşumuna sebep olmuştur. İkinci basma yükleme evresinde yeni $\pm 45^{\circ}$ kesme bantları oluşmuş ve halihazırda var olan $\pm 60^{\circ}$ kesme bantları ile girişmişlerdir. Bu kesme bantlarının girişimlerinin Mg AZ31 malzemesinin sertleşmesindeki rolü tartışılmıştır. Deformasyona dair hacimsel bilgi, birinci müşahade yüzeyine dik ikinci bir yüzün yine dijital imge korelasyonu ile incelenmesi ile elde edilmiştir. Hacimsel analiz, $\pm 45^{\circ}$ kesme bantlarının hacimsel bantlar olduğunu göstermiştir. Birincil ve ikincil inceleme yüzeylerinin imge analizi, yükleme yönünün değişmesi ile baskın deformasyon mekanizmalarının da değiştiğini göstermiştir.

TABLE OF CONTENTS

ACKNOWLEDGEMENTS iii
ABSTRACT v
ÖZET vi
LIST OF FIGURES ix
LIST OF TABLES xv
LIST OF SYMBOLS xvi
LIST OF ACRONYMS/ABBREVIATIONS xvii
1. INTRODUCTION 1
1.1. Motivation 1
1.2. Background 4
1.2.1. Slip systems in HCP metals 4
1.2.2. Twinning 6
1.2.3. Detwinning 8
1.2.4. Simple shear 9
1.3. Scope 12
2. EXPERIMENTAL METHODS 14
2.1. Sample Preparation 14
2.1.1. Texture determination 15
2.1.2. Sample geometry 16
2.1.3. Surface Preparation 17
2.1.3.1. Cold mounting 17
2.1.3.2. Grinding 18
2.1.3.3. Polishing 18
2.1.3.4. Chemical etching 18
2.1.4. DIC Speckle Pattern 19
2.2. Experimental Setup 21
2.2.1. Components 21
2.2.2. Detailed procedure 23

3. NUMERICAL ANALYSIS 26
3.1. Principles 26
3.2. Application 28
4. RESULTS 30
4.1. Stress-Strain Behavior 30
4.2. DIC Analysis 32
4.2.1. Initial compression stage 34
4.2.2. Reversal from compression - detwinning step 41
4.2.3. Transition region - High hardening ramp 46
4.2.4. Tensile Plateau 51
4.2.5. Reversal from tension 56
4.2.6. Second compression stage 59
4.2.7. Effective Poisson's ratio 63
4.2.8. Discussion 65
4.2.8.1. High angle bands 65
5. CONCLUSION 67
6. FUTURE WORK 70
REFERENCES 71

LIST OF FIGURES

Figure 1.1. (a) Unit cell for an hcp crystal, (b) basal $\{0001\}$ and type I prismatic $\{11\bar{2}0\}$ slip systems, (c) first-order pyramidal slip system, (d) second-order pyramidal slip system, (e) tensile twin system. 5

Figure 1.2. (a) Twin geometry for the $\{10\bar{1}2\}\langle\bar{1}011\rangle$ tensile twin mechanism. The c-axis of the twin band is reoriented by approximately $86°$. (b) Favorable and unfavorable loading directions for activation of tensile twin mechanism (reproduced from Kim et al. (2010) [43]). 6

Figure 1.3. (a) Compressive twin system, (b) tensile twin system for Mg and Mg alloys. 7

Figure 1.4. Shuffling of atomic positions around the twin plane resulting in twin geometries for (a) a tensile twin and (b) a compressive twin (reproduced from Guo et al. (2014) [44]). 8

Figure 1.5. (a) Tensile twin activity by resolved shear on the twin plane, (b) crystallographic orientations for the parent and twin band, (c) reversal of loading sense and detwinning by resolved shear on the twin planes inside the twin band. 9

Figure 1.6. Depiction of deformed geometries for (a) simple shear, (b) pure shear and (c) rigid body rotation processes. 11

Figure 1.7. The effect of simple shear process on the $\pm 45°$ maximum shear plane are manifested by contraction and extension in the axial and transverse directions of the uniaxial loading CS, respectively. 11

Figure 2.1. The plate coordinate system axes are defined as the rolling direction (RD), in-plane transverse direction (TD) and the plate normal (ND). Dog-bone shaped tension-compression samples are cut from the plate as shown on the TD plane. 14

Figure 2.2. Orientation distribution maps of different poles with respect to sample coordinates: $\{11\bar{2}0\}$ prismatic planes have in-plane axisymmetry, basal poles are closely aligned with the ND, and $\{10\bar{1}2\}$ pyramidal planes are about 45° away from the ND. 15

Figure 2.3. A Sketch of the sample that depicts the top surface (left) and side surface (right) view of the sample geometry. The nominal gage length of the sample is 8 mm, and the width and thickness of the EDM-machined sample are 3 mm and 3.2 mm, respectively. 16

Figure 2.4. Grain morphology and microstructure of the as-received Mg AZ31 rolled sample. 17

Figure 2.5. Iwata airbrush used for spraying. 19

Figure 2.6. Illustration of the painting process. The size of the sample is exaggerated. Painting axis is perpendicular to gravity to avoid large paint particles reaching surface. 20

Figure 2.7. Microimage of the painted surface. 20

Figure 2.8. (a) Macro-DIC optical components, (b) micro-DIC optical components, (c) Z-stage, (d) micro-tensile loading frame, (e) tensile module DAQ unit, (f) strain gage DAQ unit, (g) computer control system, (h) aluminum frame. 22

Figure 2.9. (a) Tension-compression sample, (b) LVDT transducer for displacement sensing, (c) high-strength steel power screws, (d) grips, (e) Si mirror for side surface monitoring. 22

Figure 2.10. Sample placement during the experiment. Load axis is aligned with RD. Top surface is aligned with TD and side surface is aligned with ND. The DIC regions depicted on the figure are not to scale. Sample coordinate system is defined as shown. 24

Figure 3.1. Bicubic spline interpolation of discrete data. 27

Figure 3.2. Visual illustration of the general procedure of (a) coarse search, and (b) optimization search of a DIC subset. 29

Figure 4.1. Stages of the stress-strain curve are labelled as follows: first twin plateau is TP1, detwinning ramp is DR, high-hardening ramp is HHR, tensile plateau is TensPlat, elastic region of reversal from tension is RevTens, and second compressive plateau is TP2. 30

Figure 4.2. Methodology of obtaining full-field deformation maps with microscale resolution. A uniform array of Micro-DIC frames are recorded. Their DIC results are combined to yield full-field deformation maps. Frame overlaps are not shown for clarity. 33

Figure 4.3. The geometry of simple shear processes that are at $\pm 45^{\circ}$ to the load (y) axis. ε_{yy} and ε_{xx} values are equal in magnitude with opposite senses. The magnitude of ω, is equal to principle strain values. The sign of ω changes between the opposite sense shear bands. 33

Figure 4.4. The positions of the micro-DIC analysis points on the first compressive plateau TP1: load point a is the reference state, load points $b,\ c,\ d,\ e,\ f,\ g,$ and h are on the twin plateau. 35

Figure 4.5. The combination plots for ω_{xy} obtained for points a to h. 36

Figure 4.6. The combination plots for ε_{yy} obtained for points a to h. 37

Figure 4.7. Macro-DIC results for ω fields for the top surface for points a to h. . . 38

Figure 4.8. Macro-DIC results for (a) ε_{yy} and (b) ε_{zz} fields for the side surface for points a to h. 39

Figure 4.9. ω_{xy} and ε_{yy} maps and the ε_{yy} histogram for frame (8,2) obtained for load points e and h. 39

Figure 4.10. ω_{xy} maps and ε_{yy} histograms for the selected frames obtained for load points e and h. 40

Figure 4.11. The orientations of twin planes and twinning directions for the tensile twin mechanism in rolling texture for the equally possible texture orientations (a) $\langle 11\bar{2}0\rangle$//TD and (b) $\langle 10\bar{1}0\rangle$//TD. (c) The unpreferred crystal orientation $\langle 0001\rangle$//TD. 41

Figure 4.12. Micro-DIC analysis points $i,\ j,\ k,$ and l are designated in the DR region. 42

Figure 4.13. The ω_{xy} combination plots obtained for points i to l. 42

Figure 4.14. The ε_{yy} combination plots obtained for points i to l. 43

Figure 4.15. The ω_{xy} maps and ε_{yy} histograms for the selected grids obtained for load points h and l. 44

Figure 4.16. The top surface macro-DIC ω_{xy} maps obtained for load points i to l. . 45

Figure 4.17. The side surface macro-DIC ε_{yy} maps obtained for load points i to l. . 45

Figure 4.18. Micro-DIC analysis points $l,\ m,\ n$, and o are designated in the HHR region. 47

Figure 4.19. The ω_{xy} combination plots obtained for points l to o. 47

Figure 4.20. The ε_{yy} combination plots obtained for points l to o. 48

Figure 4.21. The side surface macro-DIC ε_{yy} maps obtained for points l to o. . . . 49

Figure 4.22. The ω_{xy} maps and ε_{yy} histograms for the selected frames obtained at points l and o. 50

Figure 4.23. Micro-DIC analysis points $p,\ q$, and r are designated in the TensPlat region. 52

Figure 4.24. The ω_{xy} combination plots obtained for points p to r. 53

Figure 4.25. The ε_{yy} combination plots obtained for points p to r. 53

Figure 4.26. The side surface macro-DIC ε_{yy} maps obtained for points p to r. . . . 54

Figure 4.27. The ω_{xy} maps and ε_{yy} histograms for the selected frames obtained for load points o and r. 55

Figure 4.28. Direct observation of high angle shear band patterns due to increasing surface roughness of the top surface from point p to r at macro-DIC resolution. 56

Figure 4.29. Micro-DIC analysis points s and t designated in the RevTens region. . 57

Figure 4.30. The ω_{xy} combination plots obtained for points s and t. 57

Figure 4.31. The ε_{yy} combination plots obtained for points s and t. 58

Figure 4.32. The ω_{xy} maps and ε_{yy} histograms for the selected frames obtained for load points r and t. 58

Figure 4.33. The side surface macro-DIC ε_{yy} maps obtained for points $r,\ s$ and t. . 59

Figure 4.34. Micro-DIC analysis points $u,\ v,$ and w are on the TP2 region, load point x is the last load point of the experiment. 60

Figure 4.35. The ω_{xy} combination plots obtained for points u to x. 60

Figure 4.36. The ε_{yy} combination plots obtained for points u to x. 61

Figure 4.37. The ε_{yy} maps and histograms for the selected frames obtained for points v and w. 62

Figure 4.38. Effective Poisson's ratio computed from the macro-DIC data for the top and side surfaces. 64

Figure 4.39. The high angle shear band path microstructure characterized with smaller grain size compared to rest of the material. 66

LIST OF TABLES

Table 1.1. Primary slip systems in Mg and Mg alloys. 5

Table 2.1. Optical properties of micro-DIC and macro-DIC optics. 21

LIST OF SYMBOLS

a, c	Lattice parameters for hexagonal-close packed unit cell
C	Correlation coefficient for intensity pattern comparison
u	Displacement component in x-axis direction
v	Displacement component in y-axis direction
u_x, u_y	Partial derivative of u with respect to x and y
v_x, v_y	Partial derivative of v with respect to x and y
ε	Infinitesimal strain component
ε_M	Macroscopic (nominal) strain
ν	Poisson's ratio
σ	Stress
σ_M	Macroscopic (nominal) stress
ω	Infinitesimal rotation component

LIST OF ACRONYMS/ABBREVIATIONS

2D	Two dimensional
3D	Two dimensional
BCC	Body-centered-cubic
DIC	Digital image correlation
EBSD	Electron back-scattering diffraction
EDM	Electric discharged machining
FCC	Face-centered-cubic
HCP	Hexagonal-close-packed
ND	Neutron diffraction
RD,TD,ND	Rolling, in-plane transverse, normal directions in a rolled plate
RVE	Representative volume element
SXRD	Synchrotron X-Ray diffraction
XRD	X-Ray diffraction

1. INTRODUCTION

1.1. Motivation

Metals and ceramics are used in most engineering applications. These materials are crystalline, and in most engineering cases, used materials have a polycrystalline microstructure. The deformation and failure behavior of these materials under loading and formability during manufacturing processes depend on the aggregate behavior of the many crystals that constitute the material. Simplified deformation models assume isotropic and homogeneous elastic and plastic material behavior. In these models, all complexities regarding heterogeneity and anisotropy are thought to be averaged out at the macroscopic level. Accordingly, the material is treated as an ensemble of representative volume elements (RVE), where stress/strain are homogeneously distributed among these elements.

These approaches discount the microscopic physical aspects of deformation. The crystals that build up the structure are inherently elastically and plastically anisotropic. Macroscropic loading and deformation is mediated by a stress/strain distribution among grains. Each grain behaves coherently with the surrounding grains to sustain equilibrium and geometric compatibility in the locale. The distribution of stress/strain among the grains is bound to the relative crystallographic orientation of each grain with respect to the macroscopic loading direction and the orientation of the surrounding grains.

In a randomly textured material (i.e., grains are randomly oriented) with a highly symmetry crystal structure (e.g., body centered cubic, face centered cubic) stress/strain localizations are effectively averaged out at the macroscopic level. Simplified continuum analyses are successful in predicting the behavior of such materials. In a textured material, however, grains are preferentially oriented such that certain crystallographic axes are aligned with a sample coordinate axis. In such cases, strain must be accommodated in a certain group of grains that is most suitably oriented to undergo plastic deformation.

This localization effect is even more pronounced in materials with low-symmetry crystal structures (e.g., hexagonal-close-packed, or HCP) since easy slip systems are available for few directions. Hence, understanding the microphysics of deformation is fundamental to developing more successful models that account for the microscopic complexities of the deformation observed in these materials.

Deformation twinning is a predominant deformation mechanism substantially observed in low symmetry HCP materials [1–3]. In a twinned grain, the twin region is reoriented to become the mirror image of the rest of the crystal with respect to the twin plane. Deformation twinning induces a fixed transformation strain (13% for Mg) in a very localized manner. The lack of easy slip systems that can accommodate strain along the c-axis of an HCP crystal is compensated by deformation twinning systems (e.g., Mg exhibits heavy twinning). A twinning operation is unidirectional, that is, it operates only in a certain shearing sense but not the opposite. Its unidirectional nature also give rise to the plastic anisotropy commonly seen in Mg materials.

To understand the nature of twinning in Mg and Mg alloys, monotonic loading [4–16] and cyclic loading [5, 17–33] studies have been conducted. It has been found that, in heavily textured Mg alloys, compression along prior cold-working directions (e.g., rolling direction, extrusion direction) results in substantial twinning, and plastic deformation is governed by twinning up to high strain levels [4, 10, 11, 20, 21]. Furthermore, the material behavior shows loading direction dependency [5, 8, 32], twinning-detwinning governed deformation under cyclic loading [17, 19–21], plastic anisotropy [5, 18, 24], highly distorted hysteresis loops under cyclic loadings [28, 29], severe texture formation under loading [4, 10, 12, 13, 32], and stress concentration around twin bands [7, 13, 21]. Method-wise, diffraction studies focus on texture formation by following diffraction patterns and stress redistribution upon twinning. Electron backscattered diffraction studies, on the other hand, focus on twin band formation and the statistical aspects of twin band inception and growth in relation to microstructural parameters [14, 15]. However, a quantitative analysis of heterogeneous deformation behavior in Mg alloys under cyclic loading is absent in previous studies as will be discussed next.

Deformation heterogeneity is one of the major outcomes of twinning based deformation [34]. Strain heterogeneity directly affects the formability and failure behavior of materials. In regards to strain heterogeneity, the digital image correlation (DIC) method has proven useful (for detailed information about DIC method and extensive literature review, refer to Aydıner and Telemez (2014) [34] and Carroll et al. (2010) [35]). The DIC method yields full-field deformation maps in different materials [34, 36–41]. Specifically for Mg alloys, Hazeli et al. (2013) [36] conducted a study using an optical DIC method to investigate the effect of alloying element content on the plasticity of Mg-Al-Zn-Sr alloys. The DIC analysis revealed macroscale shear bands forming upon straining. However, the study does elaborate on the behavior of macroscopic strain heterogeneities. Aydıner and Telemez (2014) [34] conducted a study, which constitutes a foundation for the present study, where they in-situ observed two perpendicular faces of a compression sample cut from a bulk rolled plate. At sequential load steps, they monitored the primary observation face with microscopic resolution. By scanning over the entire face at each load step, they obtained full-field deformation maps at the respective load steps. The deformation maps have shown that, strain is accommodated by $\pm 45^{\circ}$ macroscopic shear bands that span the entire volume and the deformation fields are heavily heterogeneous. At a lower length scale, another $\pm 45^{\circ}$ band pattern is resolved inside the macroscale shear bands. Aydıner and Telemez (2014) successfully demonstrated that strain heterogeneities at different length scales are interlinked.

Heterogeneous deformation and reverse (or cyclic) loading performance of Mg materials have been treated separately to date. To our knowledge, there is no study that considers heterogeneous deformation effects under cyclic loading. With the scanning in-situ DIC method that yields statistically significant data, the present study intends to reveal full-field structured strain localization patterns that evolve during the course of reverse loading. Understanding the *structure* of the deformation in these materials will enable a better understanding of mechanistics and microphysics of deformation in twinning materials.

1.2. Background

1.2.1. Slip systems in HCP metals

Dislocation slip is the principal plastic deformation mechanism for most metals and ceramics. This mechanism entails dislocation glide on certain *preferred* crystallographic planes and directions. Preferred crystallographic planes and directions for dislocation slip are the densest planes and close-packed directions inside a crystal. This preference minimizes the energy cost of the dislocation core. A crystal has, in general, more than one slip system. Each slip system comprise of respective slip plane and direction. The ability of a material to undergo an arbitrary plastic strain requires the availability of at least 5 independent slip systems. The number of (easily activated) slip systems available to a material is associated with the crystal symmetry. High symmetry crystals have many slip systems. As an example, face-centered-cubic (FCC) and body-centered-cubic (BCC) crystals have 12 easy slip systems in their primary slip system family. Low symmetry hexagonal-close-packed structures have only 4 independent slip systems on near close-packed planes in close-packed directions. For HCP's dislocation glide mechanism is thus unable to meet the plastic criterion of 5 easy slip systems.

Slip systems operate when the *resolved shear stress* (RSS) on the slip plane exceeds a threshold value called *critical resolved shear stress* (CRSS). CRSS values for FCC (or BCC) systems are the same for each system due to cubic symmetry, whereas the slip systems found in HCP's might have CRSS values differing by an order of magnitude.

Figure 1.1 introduces the HCP unit cell system alongside the main slip systems encountered in Mg and Mg alloys. Figure 1.1a illustrates the inherent coordinate system used for hexagonal symmetry, where the a_1, a_2, and a_3 axes lie in the *basal* ((0001)) plane and the c-axis is normal to the basal plane. Figures 1.1b to 1.1d show the glide planes and directions of common slip systems in HCP's. Of all the presented systems, the most easily activated system is the basal slip system ($\{0001\}\langle 11\bar{2}0\rangle$), which is illustrated in Fig 1.1b. For the Mg AZ31 alloy, the reported CRSS values range from 0.8 MPa to 10 MPa [6, 42].

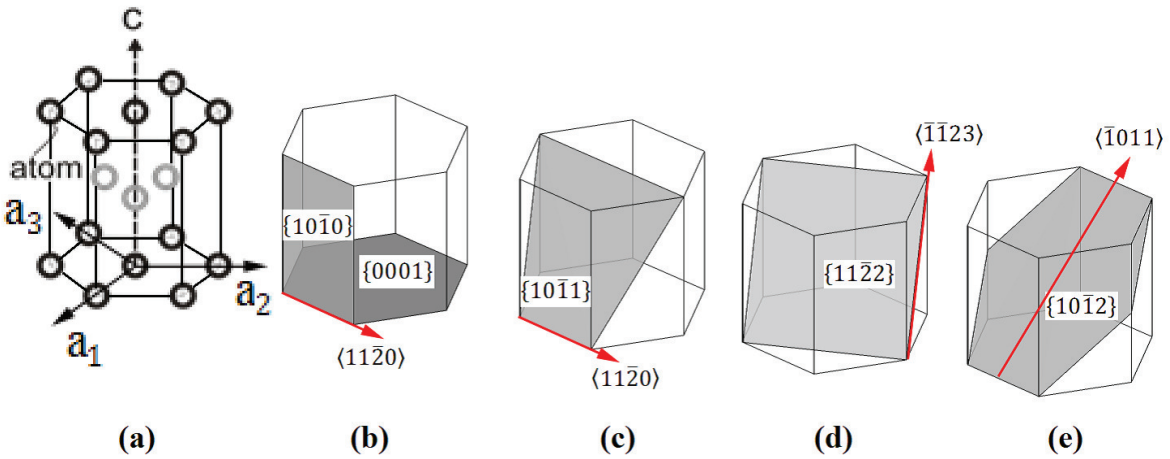

Figure 1.1. (a) Unit cell for an hcp crystal, (b) basal $\{0001\}$ and type I prismatic $\{11\bar{2}0\}$ slip systems, (c) first-order pyramidal slip system, (d) second-order pyramidal slip system, (e) tensile twin system.

The first-order prismatic slip system $\{10\bar{1}0\}\langle 11\bar{2}0\rangle$ is the second easiest slip system. With the basal systems family, they comprise 4 easy systems for Mg and Mg alloys. Harder slip systems include the first-order pyramidal (type I) $\{10\bar{1}1\}\langle 11\bar{2}0\rangle$ system and second-order pyramidal (type II) $\{11\bar{2}2\}\langle\bar{1}\bar{1}23\rangle$ system in Figs. 1.1c and 1.1d respectively. The reported CRSS values for the last two systems generally exceed 50 MPa. Still harder slip systems ($\langle c\rangle$ prismatic slip systems) are present, but are observed only under controlled single-crystal experiments [6, 42]. The slip systems are summarized in Table.1.1.

Table 1.1. Primary slip systems in Mg and Mg alloys.

Slip system no.	Burger's vector	Slip direction	Slip plane	No. of independent sys.
basal	a	$\langle 11\bar{2}0\rangle$	$\{0001\}$	2
prism (type I)	a	$\langle 11\bar{2}0\rangle$	$\{10\bar{1}0\}$	2
pyramidal (type I)	a	$\langle 11\bar{2}0\rangle$	$\{10\bar{1}1\}$	4
pyramidal (type II)	c+a	$\langle 11\bar{2}3\rangle$	$\{11\bar{2}2\}$	5
prism (type I)	c	$\langle 0001\rangle$	$\{10\bar{1}0\}$	2
prism (type II)	c	$\langle 0001\rangle$	$\{11\bar{2}0\}$	2

Only the type II pyramidal slip system, among those given in Figs 1.1b to 1.1d, generates plastic strain in the c-axis direction.

However, this system is only activated at high stresses as noted above, and when activated dissociates into sessile (immobile) components [6]. Associated with this difficulty of straining along the c-axis, the deformation twinning mechanism is commonly observed in HCP's as another mode of plastic deformation.

1.2.2. Twinning

Deformation twinning is a *transformation* process, where a part (twin band) of a crystal is reoriented into the mirror image of the rest of the crystal (matrix, parent) with respect to a *twin* plane. The reorientation action of twinning is sudden and abrupt. It dictates a certain geometry of transformation, and thus imposes a characteristic transformation strain on the structure [1, 2]. For the majority of HCP metals, the most common twinning mode is $\{10\bar{1}2\}\langle\bar{1}011\rangle$ twinning. It should be noted that, unlike dislocation slip, *shear* is not homogeneous inside a twin band, since atoms move in different directions during twinning. Figure 1.2a provides a sketch to illustrate the reorientation geometry of a Mg crystal upon twinning. For Mg, tensile twinning causes an approximately $86°$ reorientation of the c-axis of the twin region and imposes a 13% shear transformation eigenstrain [1, 2, 43].

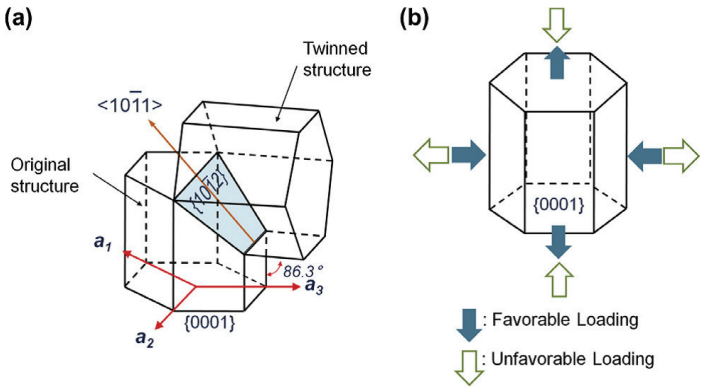

Figure 1.2. (a) Twin geometry for the $\{10\bar{1}2\}\langle\bar{1}011\rangle$ tensile twin mechanism. The c-axis of the twin band is reoriented by approximately $86°$. (b) Favorable and unfavorable loading directions for activation of tensile twin mechanism (reproduced from Kim et al. (2010) [43]).

The shearing sense of deformation twinning is unidirectional. That is, if a twin system operates under a certain direction of shearing, it does not operate in the opposite direction. This is related to the geometrical constraints of the process: the twinned part transforms into mirror image of the rest of the crystal. The activation direction of shear for HCP's depends on the unit cell parameters. For Mg the c/a ratio is 1.624, less than 1.732 (the c/a ratio that yields a square side view of the crystal) and thus the twin mechanism operates in $\langle\bar{1}011\rangle$ direction. The name *tensile twin* reflects the fact that twinning causes elongation along the parent c-axis for HCP's with a c/a ratio less than 1.732. For HCP's with a c/a ratio greater than 1.732, the $\{10\bar{1}2\}$ twin operates in the $\langle10\bar{1}\bar{1}\rangle$ direction and causes a contraction along the c-axis. Directional nature of twinning specfies the direction of loading that can trigger the twinning mechanism. Figure 1.2b portrays the favorable and unfavorable uniaxial loading cases for the $\{10\bar{1}2\}\langle\bar{1}011\rangle$ tensile twin system activation [3].

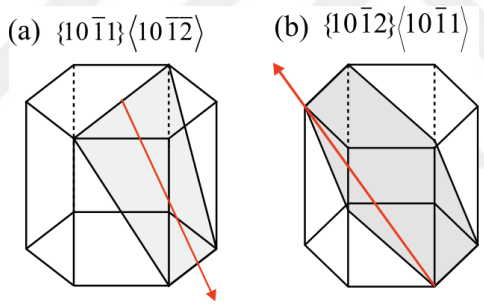

Figure 1.3. (a) Compressive twin system, (b) tensile twin system for Mg and Mg alloys.

The $\{10\bar{1}2\}\langle\bar{1}011\rangle$ tensile twin mechanism is not the only twinning mode in HCP's. Figure 1.3a shows another twin mechanism observed in HCP's. For Mg, the $\{10\bar{1}1\}\langle10\bar{1}\bar{2}\rangle$ twin is a *compressive* twin and operates in the $\langle10\bar{1}\bar{2}\rangle$ direction. However, this mechanism is very hard to activate. For Mg, the average experimentally determined CRSS value is two order of magnitude greater than that of the tensile twin system. However, pyramidal type II dislocations lead to severe hardening due to their dissociation into immobile components, and compressive twinning becomes a competitive way to strain along the c-axis under compression. Compressive twins cause a 56° reorientation of the c-axis in Mg (see Figure 1.4b).

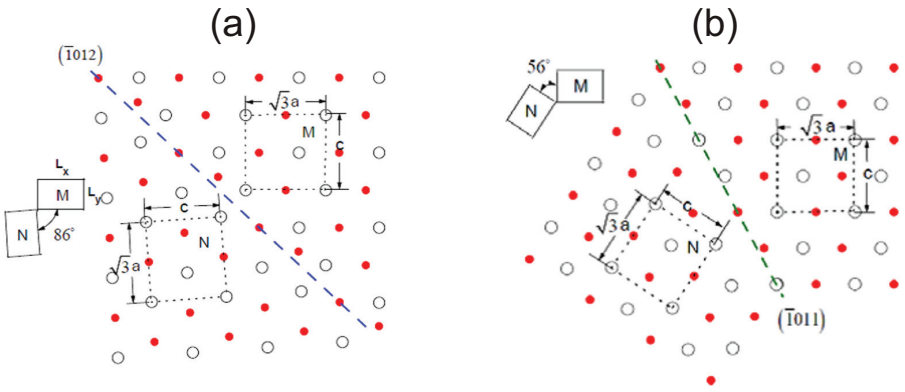

Figure 1.4. Shuffling of atomic positions around the twin plane resulting in twin geometries for (a) a tensile twin and (b) a compressive twin (reproduced from Guo et al. (2014) [44]).

The nucleation and growth of twinning, the grain size dependence of the twin mechanism and stress redistribution inside a twinning grain are heated topics of debate in twinning physics research. However, it is generally accepted that twinning causes strain relief along the c-axis of the twin band and stress redistribution between the parent grain and twin child [7, 20, 21]. It is also debated whether classical deterministic principles, such as the Hall-Petch relation and Schmid rule, are directly valid for twinning. Indeed, nucleation and growth of twins is directly affected by the surrounding grain morphology. Local factors like strain compatibility between neighboring grains and stress concentration at defect cluster sites near grain boundaries affect the behavior as much as the macroscopic loading and grain size [12, 14, 15] .

1.2.3. Detwinning

When a twinned material is loaded in the reverse direction, the twinned parts detwin in the reverse direction to the initial twinning direction. Figure 1.5 explains the mechanism behind this phenomenon. First, a Mg crystallite is compressed perpendicular to its basal $\{0002\}$ pole (Figure 1.5a), causing reorientation due to twinning. In the new shape of the twinned region, $\{0002\}$ poles are now closely oriented with the compressive loading direction (Figure 1.5b). The twin constitutes a *hard orientation* region since the c-axis in this region is now under compression.

If the macroscopic loading direction is reversed to tension (Figure 1.5c), the loading direction along the c-axis of the twin band reverses to tension too. The new loading configuration in Figure 1.5c allows *detwinning* of the twin band to its original orientation. In summary, detwinning is twinning of the twins back to their original orientation.

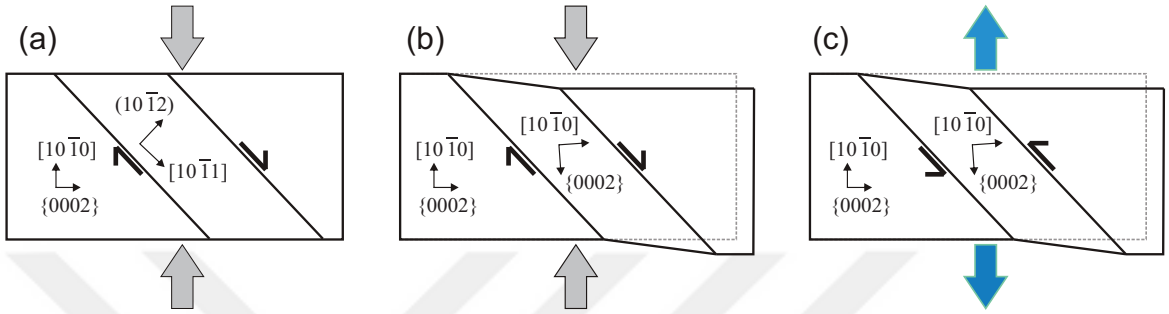

Figure 1.5. (a) Tensile twin activity by resolved shear on the twin plane, (b) crystallographic orientations for the parent and twin band, (c) reversal of loading sense and detwinning by resolved shear on the twin planes inside the twin band.

Detwinning is reported to happen at much lower macroscopic stress levels [7, 20, 21]. This is mainly due to the back stresses that developed in the twin band upon twinning. The nature of this back stress is being discussed and a consensus has yet to be reached. Synchrotron XRD measurements [7] inside individual twin-parent couples attribute the effect to the shear stress component on the twin-parent interface, whereas bulk neutron diffraction measurements [4, 11, 20] attribute this effect to the tensile back stresses along the c-axis of the twin that evolve upon twinning.

1.2.4. Simple shear

All deformation micromechanisms (dislocation glide and deformation twinning) are simple shear mechanisms. They involve gliding on crystallographic planes with a *net crystal rotation*. Figure 1.6 sketches the respective geometries of the simple shear and pure shear processes in 2D. To calculate the infinitesimal strain and rotation components, first the deformation gradients are calculated:

$$\left[\nabla u\right] = \begin{bmatrix} \frac{\partial u}{\partial x} & \frac{\partial u}{\partial y} \\ \frac{\partial v}{\partial x} & \frac{\partial v}{\partial y} \end{bmatrix} = \begin{bmatrix} 0 & \gamma \\ 0 & 0 \end{bmatrix} \tag{1.1}$$

where u and v are the displacement components in the x and y directions respectively. γ is the simple shear strain in Figure 1.6. For small strains we can write:

$$\varepsilon_{ij} = \frac{1}{2}(e_{ij} + e_{ji}) \tag{1.2}$$

$$\omega_{ij} = \frac{1}{2}(e_{ij} - e_{ji}) \tag{1.3}$$

Here ε_{ij} is the infinitesimal strain tensor and ω_{ij} is the rotation tensor. A simple shear therefore corresponds to the following strain and rotation tensors:

$$\left[\varepsilon\right] = \begin{bmatrix} 0 & \frac{\gamma}{2} \\ \frac{\gamma}{2} & 0 \end{bmatrix} \tag{1.4}$$

$$\left[\omega\right] = \begin{bmatrix} 0 & \frac{\gamma}{2} \\ -\frac{\gamma}{2} & 0 \end{bmatrix} \tag{1.5}$$

The infinitesimal strain tensor and rotation tensor add up to the deformation gradient tensor:

$$\nabla u_{ij} = \varepsilon_{ij} + \omega_{ij} \tag{1.6}$$

Figure 1.6 directly shows the above operations, and that a simple shear deformation is a superposition of pure shear and pure rotation.

The simple shear above is calculated in the *native coordinate system* of the deformation, which consists of the shear plane and its normal. Macroscopic shear planes in a polycrystalline material are the maximum shear stress planes, and they are oriented 45° away from the uniaxial loading axis.

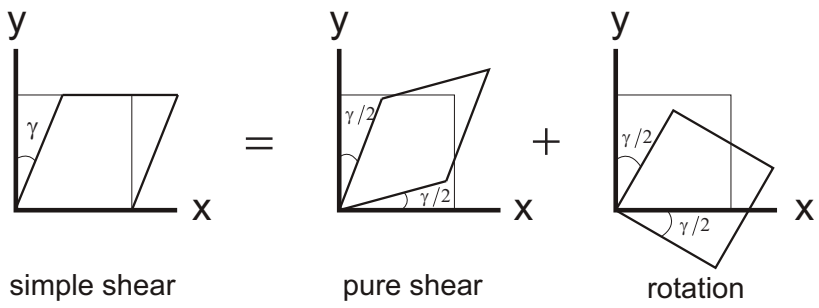

Figure 1.6. Depiction of deformed geometries for (a) simple shear, (b) pure shear and (c) rigid body rotation processes.

To find the simple shear aligned with the uniaxial loading axes (rather than the shear planes), we carry out a change of basis to rotate the coordinate system by $45°$:

$$[\varepsilon] = \begin{bmatrix} \cos 45 & \sin 45 \\ -\sin 45 & \cos 45 \end{bmatrix} \begin{bmatrix} 0 & \frac{\gamma}{2} \\ \frac{\gamma}{2} & 0 \end{bmatrix} \begin{bmatrix} \cos 45 & -\sin 45 \\ \sin 45 & \cos 45 \end{bmatrix} = \begin{bmatrix} \frac{\gamma}{2} & 0 \\ 0 & \frac{\gamma}{2} \end{bmatrix} \tag{1.7}$$

$$[\omega] = \begin{bmatrix} \cos 45 & \sin 45 \\ -\sin 45 & \cos 45 \end{bmatrix} \begin{bmatrix} 0 & \frac{\gamma}{2} \\ -\frac{\gamma}{2} & 0 \end{bmatrix} \begin{bmatrix} \cos 45 & -\sin 45 \\ \sin 45 & \cos 45 \end{bmatrix} = \begin{bmatrix} 0 & \frac{\gamma}{2} \\ -\frac{\gamma}{2} & 0 \end{bmatrix} \tag{1.8}$$

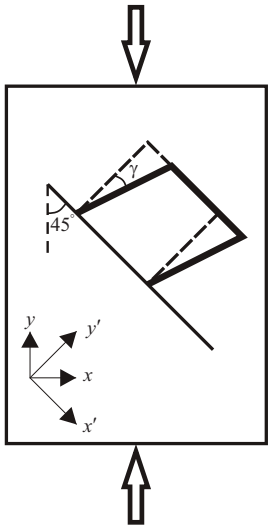

Figure 1.7. The effect of simple shear process on the $\pm 45°$ maximum shear plane are manifested by contraction and extension in the axial and transverse directions of the uniaxial loading CS, respectively.

The process of change of basis is sketched in Figure 1.7. As seen in Equation 1.8, ω is *invariant* in-plane, i.e., it stays the same with a change of basis. In the uniaxial coordinate system, our strain components for compressive loading are: $\varepsilon_{xx} = \frac{\gamma}{2}$, $\varepsilon_{yy} = -\frac{\gamma}{2}$, $\omega = \pm\frac{\gamma}{2}$ and $\varepsilon_{xy} = 0$ in the case of simple shear.

1.3. Scope

In this study, the digital image correlation (DIC) method is used to *in-situ* investigate evolution of the deformation fields and associated deformation structures, at the microscopic and macroscopic length scales, in a polycrystalline Mg AZ31 sample under fully reversed loading. The main purpose of the study is to reveal heterogeneous deformation patterns linked to twinning-detwinning activity and alternative micromechanisms in the selected material. Mg AZ31, as in the case of other Mg materials, has an easily activated tensile twin mechanism and serves as a suitable material for the study of twin physics. A tension-compression sample is cut from a rolled plate with a strong basal texture where the uniaxial loading axis coincides with the rolling direction of the plate, to enhance twin activity. In this configuration, compression along the rolling direction favors tensile twin activity, and tension along the rolling direction favors detwinning.

This study constitutes an intellectual continuation of the Aydıner and Telemez (2014) study, where deformation bands that formed in a textured Mg AZ31 sample under compressive loading were characterized at multiple scales [34]. The desired continuations of the previous study include examination of the cyclic loading behavior of the previously observed cross-band structure, and detection of anisotropic deformation mechanisms. Deformation patterns related to alternative mechanisms that activate after exhaustion of the detwinning mode are also targeted.

Two orthogonal faces of the tension-compression sample are monitored with a macro-DIC camera, and one of the faces is also monitored with a micro-DIC camera throughout the course of loading. Volumetric information regarding the deformation patterns is deduced by monitoring multiple faces.

High statistical significance is obtained by scanning over one of the examination surfaces. The microscopic examination surface is metallographically treated to reveal the granular microstructure to track possible connections between the microstructure and deformation patterns.

On the experimental side, improvements to the previous setup are introduced. A better vibration isolation system is implemented. This is expected to increase image quality significantly. The old objective lens is substituted with a new one with higher optical magnification to increase the sharpness of the images as well as the achievable range of optical magnification. The configuration of the setup is also changed. The optical axis (lens axis) in the new setup is aligned with gravity to effectively cancel some of the vibration modes that were present in the old setup. Vibration and optical improvements are expected to reduce *bias* errors intrinsic to the digital image correlation method.

2. EXPERIMENTAL METHODS

2.1. Sample Preparation

Rolled stock material of the AZ31 Magnesium alloy ($3wt\%$ Al, $1wt\%$ Zn) is procured from Alfa Aesar, USA, in the form of a 100x150x9.52 mm^3 hot-rolled plate. The Plate geometry and coordinate system is sketched in Figure 2.1. The rolling operation imposes a *crystallographic texture* in the plate material. In a textured material, the grains (crystals) that form the bulk material have preferred orientations with respect to the plate coordinate system, i.e. certain crystallographic directions of the crystals are oriented along certain plate axes.

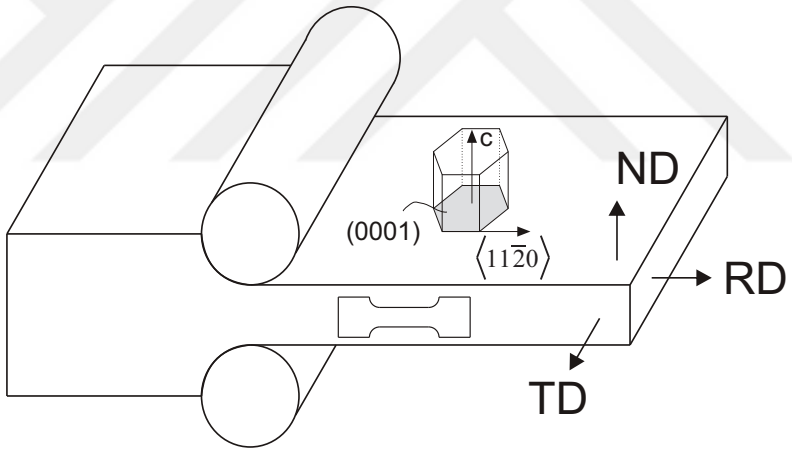

Figure 2.1. The plate coordinate system axes are defined as the rolling direction (RD), in-plane transverse direction (TD) and the plate normal (ND). Dog-bone shaped tension-compression samples are cut from the plate as shown on the TD plane.

The plate coordinate system is illustrated in Figure 2.1, showing the rolling direction (RD), in-plane transverse direction (TD) and plate normal (ND). A dog-bone cross-section of the sample cut from the plate is depicted on the same figure. The loading direction is aligned with the rolling direction (RD), whereas the main DIC observation surface normal is aligned with the in-plane transverse direction (TD).

For Mg materials, the rolling operation imposes a *basal* rolling texture on the material. The basal texture is a $\{0001\}\langle 11\bar{2}0\rangle$ texture. Here, the *basal pole* (c-axis) is aligned with the plate normal. The $\langle 11\bar{2}0\rangle$ direction, statistically, is parallel to the rolling direction. A more precise picture of the texture will be given later. Compression of the sample along RD, puts most grains under tension along the c-axis and favors activation of the $\{10\bar{1}2\}\langle\bar{1}011\rangle$ tensile twin mechanism, as explained in Figure 1.2 [45, 46].

2.1.1. Texture determination

The crystallographic texture of the as-received plate is measured with a Panalytical X-Pert Pro MPD four-cycle diffractometer. Measurements are done on a cylindrical sample with 2 cm diameter and 9.52 mm axial length. The texture of the sample is the probability of finding an orientation in units of multiples of random (MRD), where multiples of random corresponds to the normalized orientation frequency in a randomly textured material. The statistical distributions of 3 crystallographic poles are provided in Figure 2.2: the $(11\bar{2}0)$ prismatic plane, the (0001) basal plane and the $(10\bar{1}2)$ pyramidal plane.

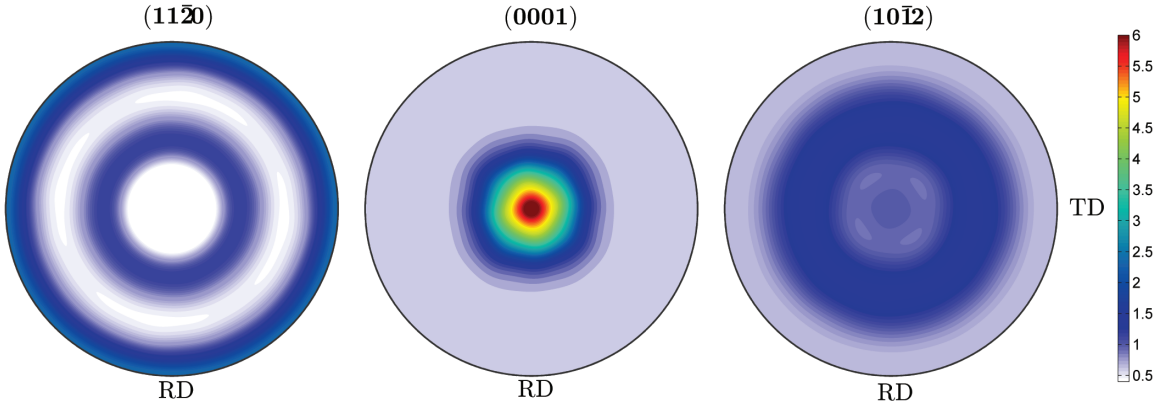

Figure 2.2. Orientation distribution maps of different poles with respect to sample coordinates: $\{11\bar{2}0\}$ prismatic planes have in-plane axisymmetry, basal poles are closely aligned with the ND, and $\{10\bar{1}2\}$ pyramidal planes are about 45° away from the ND.

Real textures display deviations from the ideal behavior. Basal poles are normally expected to be aligned with the ND, however some fraction of the grains show deviation from the ideal orientation.

The basal pole orientation of some grains strays up to 30° from the plate normal. However, nearly ideal behavior is observed. The texture has an axisymmetric texture around ND: type 1 and type 2 prismatic planes ($\{10\bar{1}0\}$ and $\{11\bar{2}0\}$ plane families) are axisymmetrically distributed around the plate normal. Pyramidal planes ($\{10\bar{1}2\}$) are oriented at 44° on average (the angle range stretches from 32° to 56°). The predominant texture also confirms that the resolved shear stress is nearly maximum on pyramidal planes during axial loading. Such texture heavily favors tensile twin activity under compression along RD due to Poisson's effect.

2.1.2. Sample geometry

Dogbone samples are EDM-machined from the rolled plate as shown in Figure2.1. Detailed sample geometry is provided in Figure 2.3.

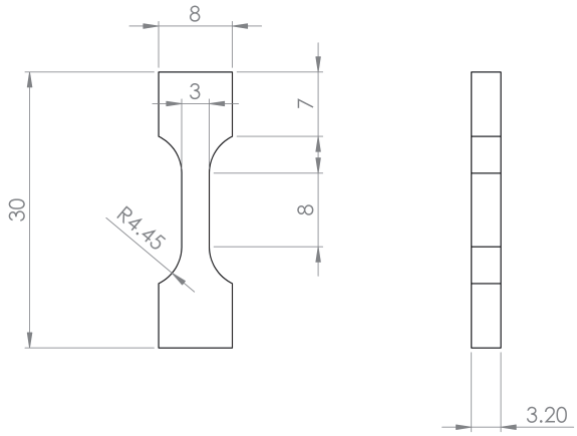

Figure 2.3. A Sketch of the sample that depicts the top surface (left) and side surface (right) view of the sample geometry. The nominal gage length of the sample is 8 mm, and the width and thickness of the EDM-machined sample are 3 mm and 3.2 mm, respectively.

To prevent any elastic buckling, the width and thickness of the sample are chosen to be similar. The cross-sectional aspect ratio is $3.2\ mm/3\ mm = 1.066$, much lower than 2.5. After metallographic preparation of the material, the thickness of the sample went down to around 2.5 mm. The aspect ratio after metallographic treatment is $3\ mm/2.5\ mm = 1.2$ which does not differ significantly from the initial value.

Hence, significant buckling is not expected. The shoulder sections of the sample are kept large and extended comparable to the gage and grip sections to ensure more homogeneous distribution of the nominal loading. Preliminary finite element simulations have shown satisfactory results. No substantial stress localization was detected at the boundary between the shoulder and gage sections.

2.1.3. Surface Preparation

To reveal the grain microstructure, the top surface of the sample (see Figure 2.3) was metallographically prepared. This helped to show the relation between strain localization and grain morphology. The Metallography process consists of mounting, grinding, polishing and chemical etching steps.

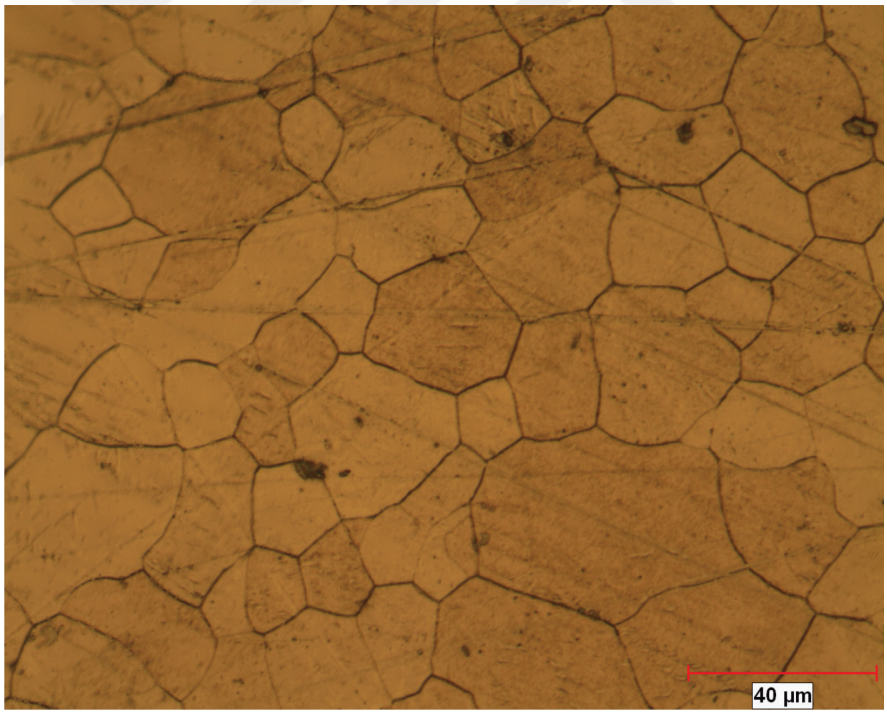

Figure 2.4. Grain morphology and microstructure of the as-received Mg AZ31 rolled sample.

2.1.3.1. Cold mounting. To ease the handling of the sample during the metallography process, the dog-bone sample was mounted in a polymer material. Mounting also ensures better surface flatness.

It also avoids extreme tapering of the sample cross-section during cutting operations. Cold mounting was used instead of hot mounting due to the practicality and ease of removal of the cold mount material after the metallographic treatment. Metkon DMT 20, which is rapidly solved by acetone, was chosen as the polymer cold mount material to further assist removal. The excess parts of the mount were cut by saw, and the resulting sample-mount couple was submerged in acetone in an ultrasonic agitator for complete removal.

2.1.3.2. Grinding. The top surface of the sample was sequentially ground with P800, P1000, P1200 and P2500 grade sandpapers. Grinding primarily removed the EDM layers which had very bad topography. For microscopic inspection the sample surface must be flat. The EDM layers were severely deformed by the local machining action and needed to be completely removed. Since Mg and Mg alloys are very soft, coarser sandpaper grades (e.g. lower than P800) did not need to be used to remove surface defects (scratches, machining traces, etches, pits, etc.). At each step, preexisting scratches from the manufacturing and metallography processes must be entirely cleaned. A classic way to do this is by turning the sample by $90°$ every 30-45 seconds turns.

2.1.3.3. Polishing. 50 nm colloidal silica is generally used to reveal grain morphology in Mg and Mg alloys. 50 nm colloidal silica is a very stable colloidal suspension of silica particles in water. During use, particles can sometimes tend to agglomerate, due to contact with ethanol. Since Mg alloys have very low corrosion resistances, 95% ethanol must be used to clean of the surface during the polishing and later stages. Using water to clean the surface leads to oxide layer formation in seconds. Surface defects that remain from the grinding steps are fully removed in this stage. A flat surface is obtained.

2.1.3.4. Chemical etching. To reveal grain boundaries, a chemical etchant is applied to the sample surface. For most Mg alloys, an acetic picral solution is used. It should be noted that the compositions of acetic picral solutions used by different researchers vary even for the same alloys. This is mainly due to the chemically very sensitive nature of Mg materials. Thus, a suitable composition for the current application needed to be found.

The used acetic picral solution was: 0.64 gr picric acid (explosive in solid form), 1.5 mL distilled water, 1.5 mL acetic acid, and 12-15 mL 99.98% quality ethanol (generally referred as *200 proof*). The surface of the sample was submerged into the acetic picral solution for 2-4 seconds.

2.1.4. DIC Speckle Pattern

For digital image correlation (DIC), characteristic surface features have to be introduced on the top and side surfaces. For conventional laboratory conditions and deformation measurement applications, one of the most common methods to introduce the characteristic *speckle* pattern is painting the surface with speckle sizes suitable for the given DIC analysis scale. For the side surface where only macroscale DIC analysis is conducted, black and white paint is coarsely applied. For the top surface, a fine mist of black paint is sprayed with an Iwata airbrush (see Figure 2.5).



Figure 2.5. Iwata airbrush used for spraying.

The speckle size for microscale DIC should be commensurate with the length scale of the deformation measurement. For an intra-grain measurement resolution, the speckle sizes must be much smaller than the grain size. The DIC method searches for *patches* of pixels in undeformed and deformed images. Accordingly, the speckle pattern should be smaller than the patch size used for the DIC method. The DIC method will be explained in detail later.

The application of fine mist directly onto the top surface needs careful adjustment. Blowing fine mist from a close distance results in coarse speckles. Blowing from far distances may not achieve the required feature sizes. Thus, the spraying distance should be optimized. Similarly, the spraying pressure should be adjusted. In this study, black point-water solution is sprayed from a distance of 10 cm with a pressure of 4 bars.

The procedure is sketched in Figure 2.6.

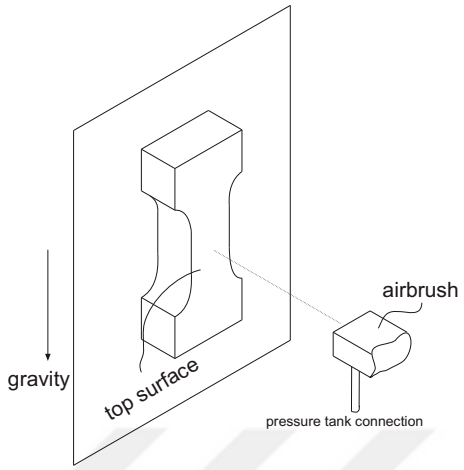

Figure 2.6. Illustration of the painting process. The size of the sample is exaggerated. Painting axis is perpendicular to gravity to avoid large paint particles reaching surface.

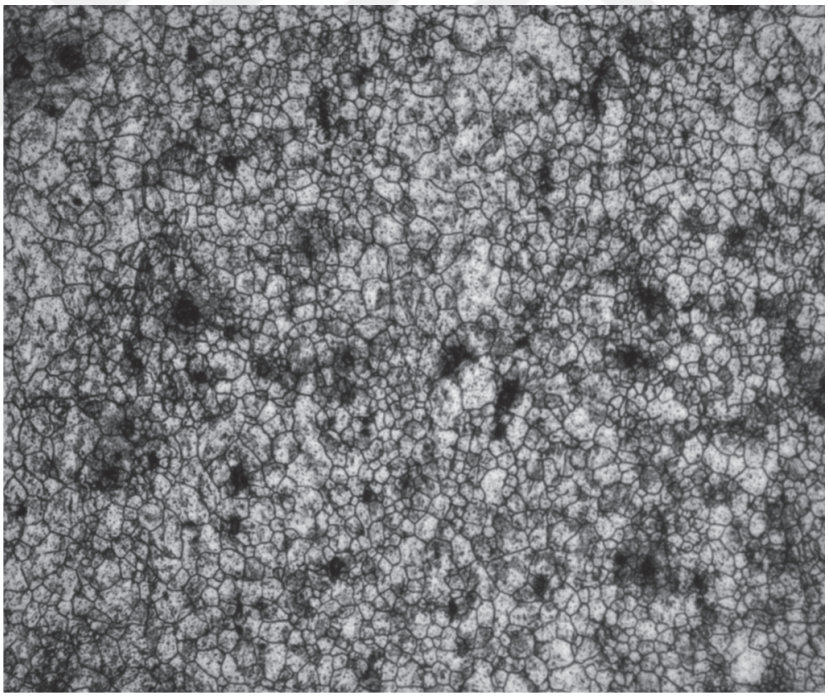

Figure 2.7. Microimage of the painted surface.

A sample frame after painting the top surface is shown in Figure 2.7. Although agglomerated paint points exist, most grains are painted with speckles with sizes about 1/20 of the grain diameter.

2.2. Experimental Setup

2.2.1. Components

The experimental setup used in the study comprised the following elements: the tensile module, micro-DIC and macro-DIC optics, positioning system, vibration isolation table, an aluminum frame, and a computer control system. The tensile module is Kammrath $\&$ Weiss micro-tensile module equipped with a 10 kN load cell. Newport-ILS series linear stages with $0.5\mu m$ resolution are combined to compose the positioning system. The positioning system is controlled by a computer code via a Newport controlling system. Both micro-DIC and macro-DIC systems use AVT Pike F505B cameras. An Edmund Optics $0.5\times$ telecentric lens is fitted to the macro-DIC camera. For the micro-DIC optics, a combination of an adapter part, a zoom lens (Navitar 60191D with coaxial lighting) and an objective lens (Mitutoyo infinity corrected lens with $10\times$ magnification) is used. The resulting optical properties (optical resolution, working distance and depth of field) and frame dimensions are summarized below in Table 2.1.

Table 2.1. Optical properties of micro-DIC and macro-DIC optics.

DIC scale	Optical resolution	WD	DOF	Frame dimensions	CCD Sensor
micro-DIC	$0.19\ \mu m/pixel$	$35\ mm$	$7\ \mu m$	$0.465\ \mu m \times 0.39\ \mu m$	2452×2054 pixels
macro-DIC	$6.8\ \mu m/pixel$	$110\ mm$	$2\ mm$	$16.7\ mm \times 14\ mm$	2452×2054 pixels

An image of the experimental setup is given in Figure 2.8. Micro-DIC and macro-DIC optics hang on the aluminum frame and are fixed. The tensile module is placed on the Z-stage which, in turn, is placed on the X-Y stages. This configuration reduces vibration effects by minimizing the cantilever length of all components perpendicular to gravity. Hence, better image quality is ensured. The strain gage data acquisition unit, shown in Figure2.8f, is used for close tracking of the yielding point. Strain gage data is not used for later stages, since macro-DIC results are used for nominal deformation measurement.

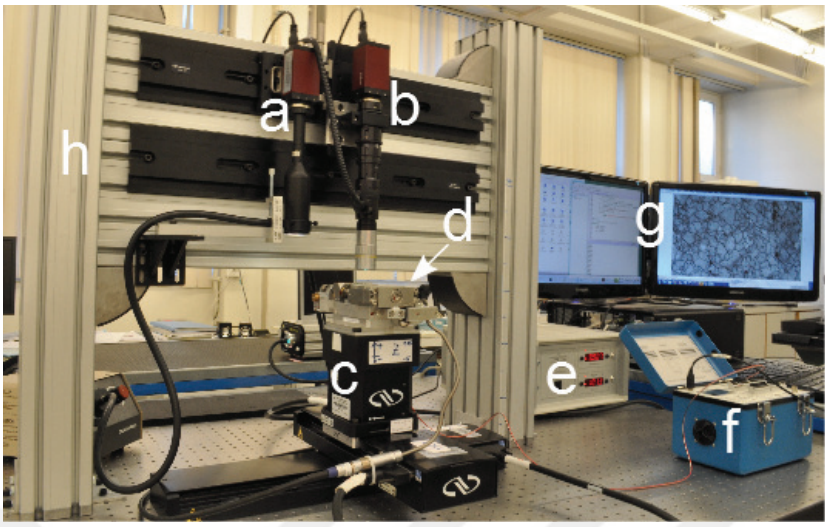

Figure 2.8. (a) Macro-DIC optical components, (b) micro-DIC optical components, (c) Z-stage, (d) micro-tensile loading frame, (e) tensile module DAQ unit, (f) strain gage DAQ unit, (g) computer control system, (h) aluminum frame.

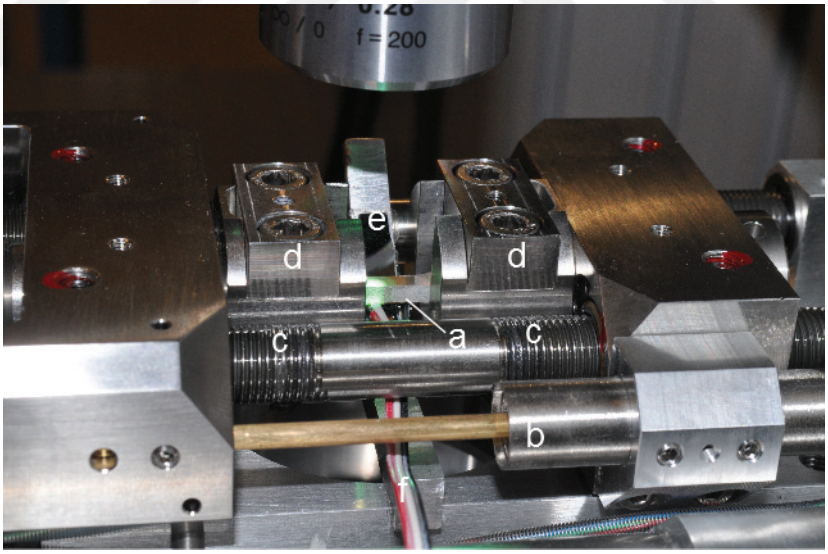

Figure 2.9. (a) Tension-compression sample, (b) LVDT transducer for displacement sensing, (c) high-strength steel power screws, (d) grips, (e) Si mirror for side surface monitoring.

The test sample is installed on the tensile module with *strain relief*. This is done by stepwise tightening of the grip screws (shown in Figure 2.9d). The sample is placed in the grips (Figure 2.9a).

Then the upper grips are slightly tightened, and preloading from the tightening is monitored by the load cell DAQ. The sample is relieved by small increments of tensile or compressive loading, depending on the preloading from the tightening the grips. Gliding of the sample from the grips is avoided.

A single-crystal Si deposition mirror oriented 45° away from the vertical axis is used for side surface monitoring, as shown in Figure 2.9e. This is needed since the macro-DIC optics are fixed on the aluminum frame and the vertical axis is perpendicular to the top surface. Proper lighting is needed for both macro-DIC and micro-DIC optics. For the macro-DIC optics, a specular lighting fiber is fitted as shown in Figure 2.8a. For the micro-DIC optics, a coaxial lighting fiber is fitted the the zoom lens. The fiber that is attached to the micro-DIC optics is seen in Figure 2.8b, and the coaxial light incident on the sample is shown in Figure 2.9a.

2.2.2. Detailed procedure

Before starting the experiment, a *no strain rigid body translation experiment* is conducted to test the quality of the DIC-pattern and to characterize the systematic error in strain measurement from algorithmic and experimental sources. The rigid body translation experiment involves comparing two images taken sequentially at slightly displaced positions. For this, a microscopic image is taken at an arbitrarily chosen point of the sample surface. Then the tensile frame is translated by a small distance (say by 1 pixel) in direction, then microscopic image of the surface at new position is taken again. Comparison of the two images should ideally yield rigid body displacement result with no associated strain. A Dirac-delta like (sharp peak with low standard deviation) histogram of strain centered around the input displacement value signifies satisfactory result. Details of the DIC method used will be given later.

The loading is started after checking rigid body translation conditions. At the beginning, macroscopic images of the top and side surface are taken, and micro-DIC scan is performed.

The micro-DIC scan involves taking micro-images of the frames inside the micro-DIC grid. The micro-DIC grid is a 20×6 array of adjacent micro frames that span most of the top surface area when combined. It is defined by the (x,y) positions (for linear stages) of the frame centers. Using a Python script through which both DIC-optics and positioning systems are controlled, the entire micro-DIC grid is scanned, and a sharp (in-focus) image of the frame is taken at each frame center position. Due to the topography of the surface, or the taper of the top cross-section, each frame may not be imaged in focus at the same Z-position of the stages. To ensure focus quality of the micro-images, an autofocusing operation is performed at each frame. Autofocusing entails taking images of a frame at very closely spaced Z positions, then comparing the sharpness of these images and selecting the sharpest one. The sharpness of the images are evaluated with the appropriate focus measure [47].

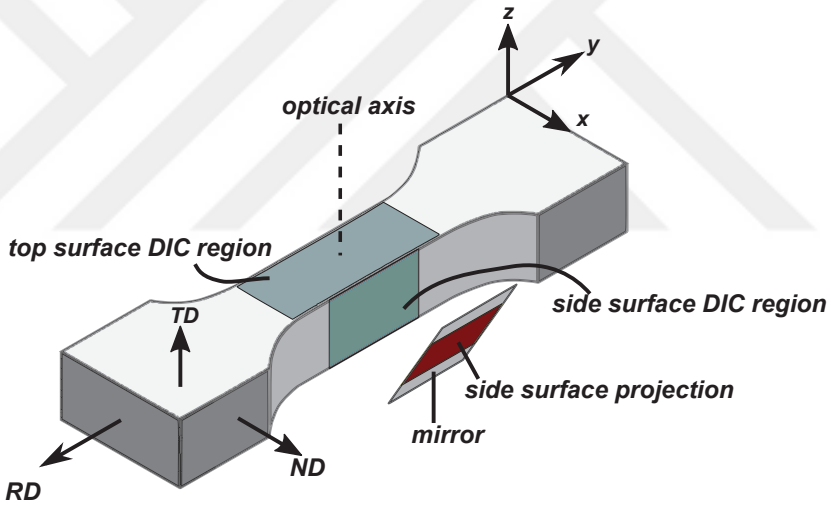

Figure 2.10. Sample placement during the experiment. Load axis is aligned with RD. Top surface is aligned with TD and side surface is aligned with ND. The DIC regions depicted on the figure are not to scale. Sample coordinate system is defined as shown.

After the initial setting and taking the undeformed images, the load is increased by small increments. At each load step macro-DIC images are taken. The nominal strain at each load step is measured using the macro-DIC analysis of the top surface images. The nominal strain is then supplied to the micro-DIC routines to recalculate the micro-DIC grid center positions. Note that, with the increased load, the macroscopic shape of the sample is uniaxially deformed. This causes shifting of the frames in the micro-DIC grid due to the nominal strain.

The frame center positions are recalculated by accounting for the shifting of the grids. Having defined the updated micro-DIC grid, microscopic images of each frame in the grid are taken (micro-DIC scan). After finisihing the micro-DIC scan, load is incremented again and the procedure is repeated.

The entire procedure explained above is automated and controlled from a central Python script, except for application of the load. Load application is done manually.

A noteworthy point is that frames that the constitute the micro-DIC grid overlap. Overlapping frames are desired since when loading is introduced some material points in the undeformed images leave the frame regions due to the rigid body translation and local deformation effects. To minimize data loss in this situation, two neighboring frames share an overlapping region. Overlap distances are 400 pixels in both the x and y directions.

3. NUMERICAL ANALYSIS

3.1. Principles

Deformation measurement via digital image correlation (DIC) is based on matching the image intensity patterns to uniquely identify material regions. In the DIC method, the deformed image of the sample surface is compared to its image at the reference state. Specifically for the DIC algorithm used in this study, the displacements (u, v) and spatial first order displacement derivatives ($\partial u/\partial x$, $\partial u/\partial y$, $\partial v/\partial x$, $\partial v/\partial y$) are measured at each point of an array of closely spaced grid points (x,y). To measure the displacement and first order derivatives at a grid point, the deformed state is searched for a grayscale intensity pattern over a subset of pixels around the grid point in the reference state. Physically, when deformation occurs, a material point at (x, y) is displaced to (x^*, y^*) in the deformed image. The deformed coordinates can be expressed in terms of the initial coordinates as follows:

$$x^* = x + u(x, y) \tag{3.1}$$

$$y^* = y + v(x, y) \tag{3.2}$$

Let the grayscale intensity value at the initial state and the deformed state be $I(x, y)$ and $I^*(x^*, y^*)$. In the ideal case of pixel searching these two intensity values match ($I(x, y)$ should be equal to $I^*(x^*, y^*)$). However, the pixel intensity at a point is not unique, since in an 8-bit grayscale image a pixel can only have an integer intensity value between 0 and 255 (0 is black, 255 is white). Therefore to ensure a unique search, a *subset / patch* of pixels around a subset center (x_0, y_0) is tracked. This patch of sufficient size contains a unique intensity distribution, the coordinates of an arbitrary point in the deformed state can be approximated by a first order Taylor expansion about the grid point as follows:

$$x^* = x + u(x_0, y_0) + \frac{\partial u(x_0, y_0)}{\partial x}(x - x_0) + \frac{\partial u(x_0, y_0)}{\partial y}(y - y_0) \tag{3.3}$$

$$y^* = y + u(x_0, y_0) + \frac{\partial v(x_0, y_0)}{\partial y}(y - y_0) + \frac{\partial v(x_0, y_0)}{\partial x}(x - x_0) \tag{3.4}$$

The parameters to be determined are the coefficients of above equations:

$$u = u(x_0, y_0) \qquad v = (v_0, y_0) \tag{3.5}$$

$$u_x = \frac{\partial(u_0, y_0)}{\partial x} \qquad u_y = \frac{\partial(u_0, y_0)}{\partial y} \tag{3.6}$$

$$v_x = \frac{\partial(v_0, y_0)}{\partial x} \qquad v_y = \frac{\partial(v_0, y_0)}{\partial y} \tag{3.7}$$

These values are obtained at the subset centers. However, the intensity pattern over the subset in the deformed state does not exactly match the intensity pattern in the reference state due to experimental imperfections and physical conditions. First, the two images cannot be taken at the same conditions, leading to inevitable minute changes. Second, pixels of the deformed subset might deform by a fraction of a pixel, causing the deformed coordinates (x^*, y^*) to not correspond to a discrete pixel coordinate in the deformed image. This second phenomenon necessitates one more procedure: the discrete deformed image data must be interpolated to yield a continuous intensity field to achieve sub-pixel resolution. Otherwise, intensity values at (x^*, y^*) could not be used as they are generally non-integer values. A bi-cubic spline interpolation scheme is used for the interpolation operation, and the deformed images are converted into continuous fields (as depicted in Figure 3.1).

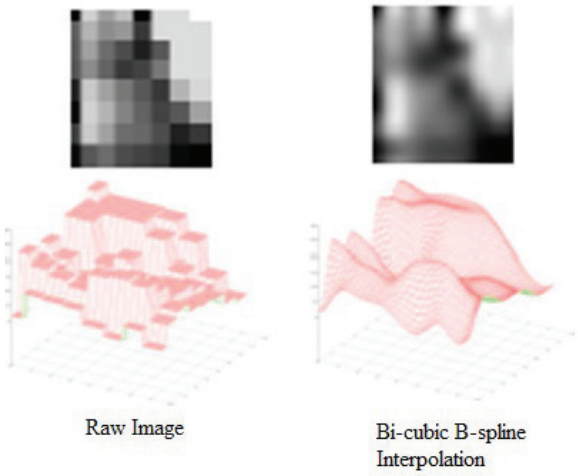

Figure 3.1. Bicubic spline interpolation of discrete data.

Given the DIC-grid and (x, y) coordinates of the subset centers, the (x^*, y^*) coordinates are sought.

To find them, the difference correlation between intensity patterns should be minimized (exact matching is impractical). A correlation coefficient that quantifies the difference between deformed and reference state subset patterns is defined as follows:

$$C = \sum_{i=1}^{N} [I(x, y) - I(x^*, y^*)]^2 \tag{3.8}$$

Here C is defined as the correlation coefficient for each subset pattern where the intensity square sum is indexed over the pixels inside the subset and N is the number of pixels inside the subset. Note that there are alternative correlation coefficients [48]. The correlation coefficient is minimized to find the subset mapping.

3.2. Application

Figure 3.2 explains how DIC principles are applied to the deformation measurement problem. First a *DIC grid* is defined (Figure 3.2a, left) as an array of subset center points for which the displacements and their first derivatives will be determined. Next, at each grid point (say the point with red square subset region in Figure 3.2a) a coarse search operation is performed. For this, the subset is searched for in a *search grid* (yellow region in Figure 3.2a, right). The coarse search step, considers only translation, that is, $\frac{\partial u}{\partial x}$, $\frac{\partial u}{\partial y}$, $\frac{\partial v}{\partial x}$, and $\frac{\partial v}{\partial y}$ are assumed to be zero. The reference state subset is compared with subsets around the search grid points. The search grid point, that minimizes the correlation coefficient, is temporarily selected as the grid point with highest correlation. Then a second and smaller search grid is defined around this point and the coarse search procedure is repeated. Similarly, after the second coarse search step third and fourth coarse search steps are performed. At each step the grid point with highest correlation is selected, as the search grid is constricted to smaller regions and the distance between search grid points is reduced by a certain fraction. At the end of the last coarse search step, the correct position of the subset is found to within one pixel.

Sub-pixel resolution is achieved by the subsequent fine (optimized) search, Figure 3.2.

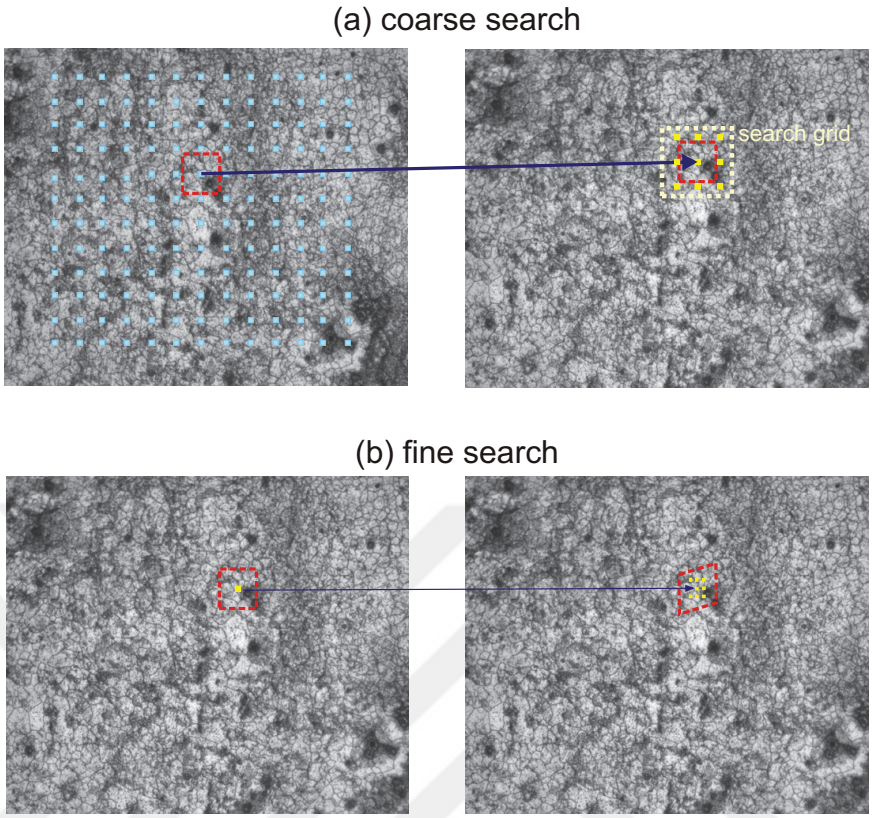

Figure 3.2. Visual illustration of the general procedure of (a) coarse search, and (b) optimization search of a DIC subset.

This step first optimizes u and v values around those determined from the coarse search while keeping the other variables constant. The same procedure is repeated for u_x and v_y, and then for u_y and v_x. For each variable couples, other sets of parameters are held constant. The optimization scheme follows a Newton-Raphson optimization algorithm. Note that the search grid shown for fine search in Figure 3.2b is exaggerated for visibility. In fact, the trial u and v values are within one pixel. For further details of the DIC method and applications, please refer to Chu et al.(1985)and Vendroux (1998) [49, 50].

For the micro-DIC analysis, 61×61 pixel subsets ($\sim 12\ \mu m \times 12\ \mu m$) are used. Grid points (subset centers) are separated by 10 pixels. 81×81 pixel subsets ($0.55\ mm \times 0.55\ mm$) and 10 pixel spacing is used for the macro-DIC analysis.

4. RESULTS

4.1. Stress-Strain Behavior

The sample is loaded through a reversed loading cycle which starts with an initial compression stage. Macroscopic DIC data is used to measure total strain (ε_{yy}). The total strain is calculated as:

$$\varepsilon_M = |\overline{\varepsilon}_{yy}| \tag{4.1}$$

where ε_{yy} are measured longitudinal strain values for each subset center point of the macro-DIC grid as described in the Section 3.2 [34].

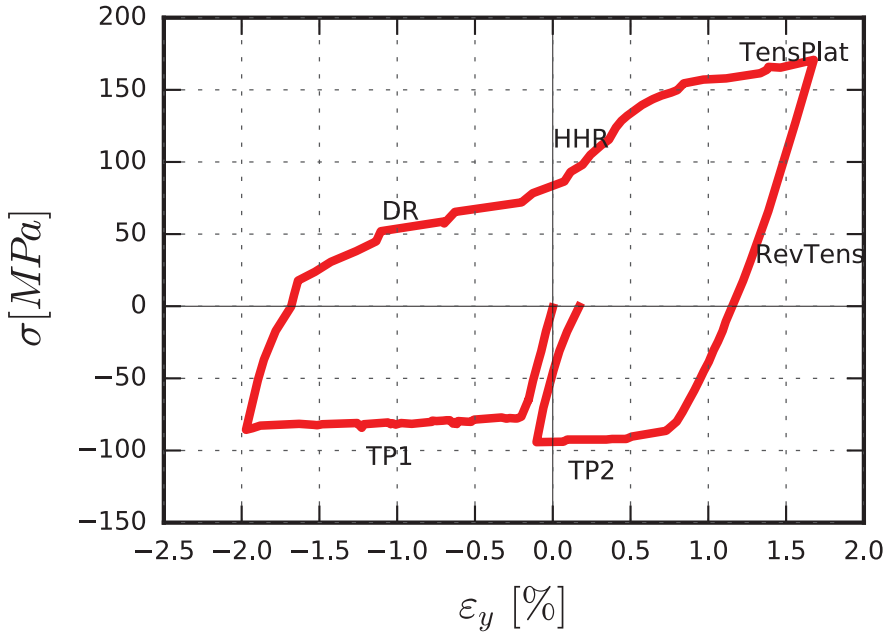

Figure 4.1. Stages of the stress-strain curve are labelled as follows: first twin plateau is TP1, detwinning ramp is DR, high-hardening ramp is HHR, tensile plateau is TensPlat, elastic region of reversal from tension is RevTens, and second compressive plateau is TP2.

The stress-strain curve of the experiment is provided in Figure 4.1.

Initially, strain is increased incrementally with a nominal 0.03% step size. The strain increments are increased after the first twin plateau (TP1) is reached at around $\varepsilon_M = -0.25\%$ ($\sigma_M = -82$ MPa). The sample is compressed to a -2% strain in the TP1 region. A serrated flow behavior is observed in this stage. After reaching -2% strain, the sample is loaded in the reverse direction. Three different stages are traversed during reverse loading, named 'detwinning ramp', 'high-hardening ramp' and 'tensile plateau'. The region labels are assigned based on well-known micro-mechanistic behavior in the respective regions [5, 19, 20, 24, 26, 27, 32]. Accordingly, twinning dominates the plastic range on the compression stage and detwinning provides compressive strain recovery during the first stage of reverse loading until around 0% strain. During the high hardening ramp, 'HHR', dominant deformation mode is changed from detwinning to higher order plastic mechanisms such as type I pyramidal slip and compressive twinning [19, 26, 27].

The stress-strain curve of the experiment exhibits a '*sigmoidal*' shape. This shape is characteristic of twinning materials [5, 8, 18, 20, 24, 27, 29], and is related to the aforementioned mechanism changes that take place in the course of reversed loading. For the present texture, compression along rolling direction favors $\{10\bar{1}2\}\langle\bar{1}011\rangle$ tensile twin activation. The tensile twin mode is relatively easy for Mg AZ31 among all other deformation mechanisms, only slightly harder than basal slip [42]. The unloading is non-linear since detwinning starts immediately upon unloading. However, unloading is still predominantly elastic and detwinning remain limited until an unstressed state is reached. Afterwards, loading in tension facilitates further detwinning. The increased activity of detwinning is evident in the *detwinning ramp*, that exhibits low hardening, i.e., relatively flat stress-strain curve in DR, Figure 4.1. Towards the end of the detwinning region, the stress-strain curve start to change shape from concave to convex. The shape change marks the end of detwinning mode around the unstrained state. Further tensile straining causes high-hardening since most of the grains are oriented in hard directions i.e., their basal planes are perpendicular to the imposed loading and they are compressed along their c-axes. Such a configuration leads to severe stress build-up in the '*high hardening ramp*'. This region can also be referred to as a '*transition region*' since the deformation mode changes from detwinning to harder deformation modes.

Plastic deformation in the '*high hardening ramp*' and further stages necessitates activation of harder mechanisms. This explains why '*tensile plateau*' begins at a much higher stress value than the *twin plateau* and the observed *plastic anisotropy*. Hard deformation modes sustain further straining in the *tensile plateau*. After reaching $\varepsilon_M = 1.6\%$ strain, the sample is unloaded again. The sample is once more loaded in compression after the unload, starting the second cycle. The second twin plateau (TP2) starts around -89 MPa. Compared to the -82 MPa value of TP1 stress level, this entails a cyclic hardening of around 8%. The second twin plateau (TP2) also shows a serrated stress-strain behavior. The strain bursts observed in TP2, however, are milder compared to those of TP1, with smaller load drop magnitudes. The load cycle is ended at -0.7% strain where the sample is fully unloaded. The physical details of the deformation patterns pertaining to each loading stage will be investigated in the following sections.

4.2. DIC Analysis

Each distinct stage of the reverse loading path is investigated with DIC analysis in this section. Contour plots are used to convey spatial distribution of strain while histograms are used for quantitative evaluation of the strain data.

Top surface deformation patterns are presented with both microscopic and macroscopic DIC resolution. On the other hand, DIC with only macroscopic resolution has been implemented on the side surface. Top and side surface are evaluated together to deduce volumetric information about the deformation patterns. Top surface DIC contour plots will have three formats: (i) macro-DIC frames at macroscopic DIC resolution for which compared images contain the entire gage section (Section 2.2.2, Figure 2.3), (ii) individual micro-DIC frames that present crystallite-level strain structures, (iii) combination plot of the micro-DIC frames that nearly matches the field of the macro-DIC frame. The combined micro-DIC frames are recorded over a 20x6 grid sketched in 4.2. The combination plots are used to bridge microscopic and macroscopic length scales for deformation structures. Bulk of the presented results are in this format.

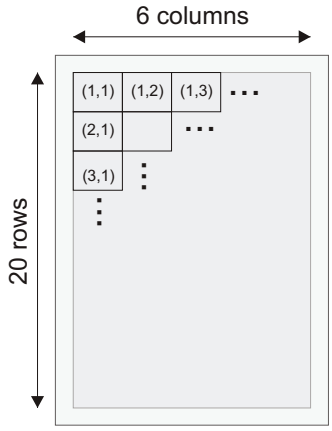

Figure 4.2. Methodology of obtaining full-field deformation maps with microscale resolution. A uniform array of Micro-DIC frames are recorded. Their DIC results are combined to yield full-field deformation maps. Frame overlaps are not shown for clarity.

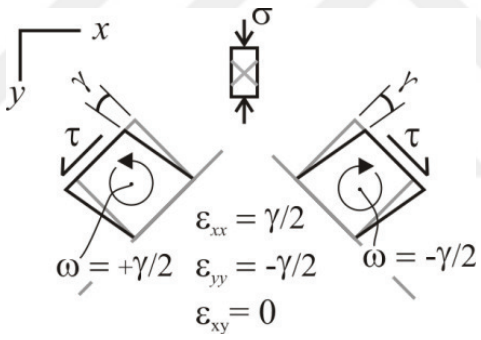

Figure 4.3. The geometry of simple shear processes that are at $\pm 45^{\circ}$ to the load (y) axis. ε_{yy} and ε_{xx} values are equal in magnitude with opposite senses. The magnitude of ω, is equal to principle strain values. The sign of ω changes between the opposite sense shear bands.

Axial strain (ε_{yy}) and infinitesimal in-plane rotation component (ω) are chosen as the contour plot variables. Using ω as the plotting variable to describe the deformation field is incorrect in general terms. However, if the deformation consists of simple shear processes whose plane of shear matches the observation surface, ω plots show strain structures with an advantage over strain components ε_{yy} and ε_{xx}: Rotation ω distinguishes the sense of simple shear processes (Figure 4.3) while strain components do not. . Also, ω is invariant in the plane and always represent the principal strain value regardless of the orientation of the shear band, which is not the case for ε_{yy} or ε_{xx}.

However, rotation ω results will be misleading when deformation deviates from the very structured form of individual shear bands with plane of shear matching the observation plane. Since ω values of the opposite sense simple shear bands (e.g., $+45^\circ$ and -45° bands shown in Figure 4.3) have opposite signs, the rotations they impose cancel when they act on the same region. Consequently, ω maps show no-rotation at these localities which can be incorrectly interpreted as no-deformation sites. In addition to this, a bias is introduced to ω by the rigid body rotation of the locality. Thus, ε_{yy} plots are used alongside with ω plots to present the real deformation field and to keep eye on regions ω loses applicability as a deformation variable. Until then, ω maps tend to distinguish individual shear processes better than strain maps.

4.2.1. Initial compression stage

The first twin plateau TP1 onsets at around $\sigma_M = -82$ MPa. Serrated stress-strain behavior is observed on the twin plateau in Figure 4.4. Macroscopic DIC data is collected at closely spaced load points. Microscopic DIC data is collected only at particular points. These *micro-DIC* data points from *a* to *h* are labelled on the stress-strain curve in Figure 4.4.

Full-field (combination) infinitesimal rotation (ω_{xy}) and axial strain (ε_{yy}) maps obtained at micro-DIC data points are provided in Figure 4.5 and Figure 4.6 respectively. Heavy strain localization at macroscale in the form of $\pm 45^\circ$ shear bands are discerned on the ω_{xy} maps in Figure 4.5. Strain is accommodated by these sharp shear bands until the end of the twin plateau. The labelled micro-DIC data points are selected to cover the major shear banding processes. At point b ($\varepsilon_M = -0.28\%$), three $+45^\circ$ (red, one of them is major) and two -45° (blue) bands are present. The remaining material is virtually undeformed. From point b to e, the major $+45^\circ$ band expands in a *cascaded* manner. All the deformation from point b to e is predominantly accommodated by this band. Each advance of the shear band is sudden and abrupt, and they are accompanied by load drops of about $3 - 4$ MPa. These load drops yield the previously mentioned serrated stress-strain behavior in TP1. The second major $+45^\circ$ band appears at point f. By point g, in addition to the expansion of existing $+45^\circ$ shear bands, a -45° shear band emerges on the upper right side of the sample.

And a $-45°$ blue band appears inside a pre-existing $+45°$ band on the lower left side of the sample. At point h, all existing $\pm 45°$ bands expand further.

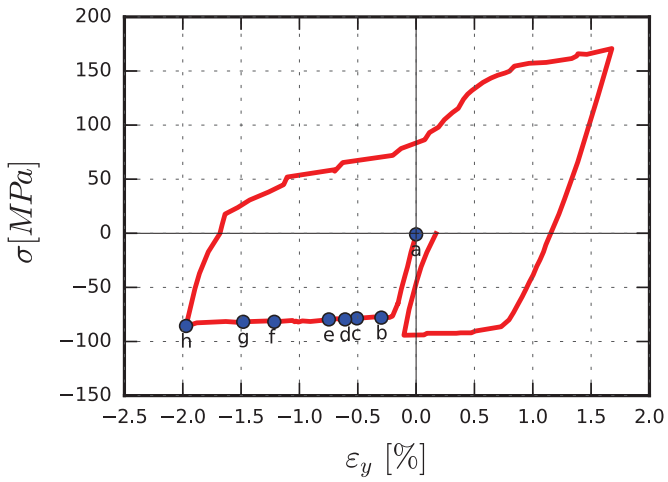

Figure 4.4. The positions of the micro-DIC analysis points on the first compressive plateau TP1: load point a is the reference state, load points $b,\ c,\ d,\ e,\ f,\ g$, and h are on the twin plateau.

The strain localization pattern observed in Figure 4.5 and Figure 4.6 is similar to the simple shear processes depicted in Figure 4.3. Accordingly, the $\pm 45°$ patterns appear on both ω_{xy} and ε_{yy} maps with identical geometry. The sense of the shear bands is distinguished on the ω_{xy} maps only, which is perfectly consistent with the simple shear geometry explained in Section 4.2. The results at macroscopic resolution also confirm these findings: Figure 4.7 gives the macro-DIC ω_{xy} maps where the cross-pair $\pm 45°$ shear band patterns are evident at the macroscopic length scale as well. For most typical deformation processes, the strain localization patterns are expected to be smeared out at the macroscopic length scale due to intermingling of the microscale simple shear processes (slip, twinning, etc.). For the present case, the simple shear patterns are sustained even at the macroscale. The rotation components of the $+45°$ and $-45°$ macroscopic bands exhibit the typical rotation cancellation when they meet. Notice, e.g., the regional cancellation of the rotation of the bottom $+45°$ shear band (red) by the $-45°$ shear band (blue) that emerges on the bottom right side of the sample, from load point d to e in Figure 4.7.

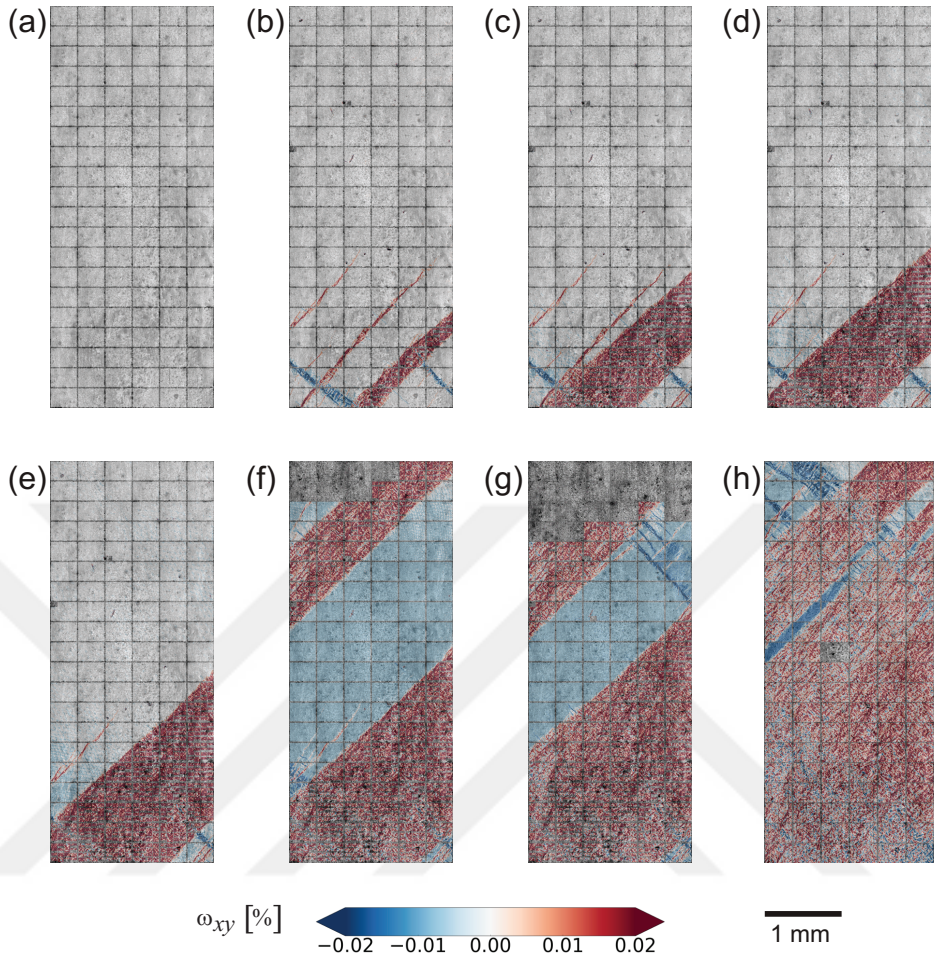

Figure 4.5. The combination plots for ω_{xy} obtained for points a to h.

Figure 4.8 gives the ε_{yy} and ε_{zz} maps over the side surface with macro-DIC resolution. Side surface ε_{yy} maps (Figure 4.8a) shows the volumetric traces of the top surface bands if they are extruded into the page (z-direction, Figure 2.3). To visualize, note the blue horizontal band on the side surface ε_{yy} map nucleates and and expands concurrently with the nucleation and expansion of the major $+45^\circ$ shear band on the bottom side of the top surface. The observed side surface band covers precisely the same region with the corresponding top surface band's intersection of the side surface. Meanwhile, the side surface ε_{zz} maps yield virtually zero strain in the z-direction (Figure 4.8b). The material is strained only in the $x-y$ plane which is perfectly consistent with the simple shear picture, where $\varepsilon_{yy} = -\varepsilon_{xx}$ (Figure 4.3) and $\varepsilon_{zz} = 0$ due to conservation of volume in plastic processes. In summary, $\pm 45^\circ$ shear bands are not just features on the top surface.

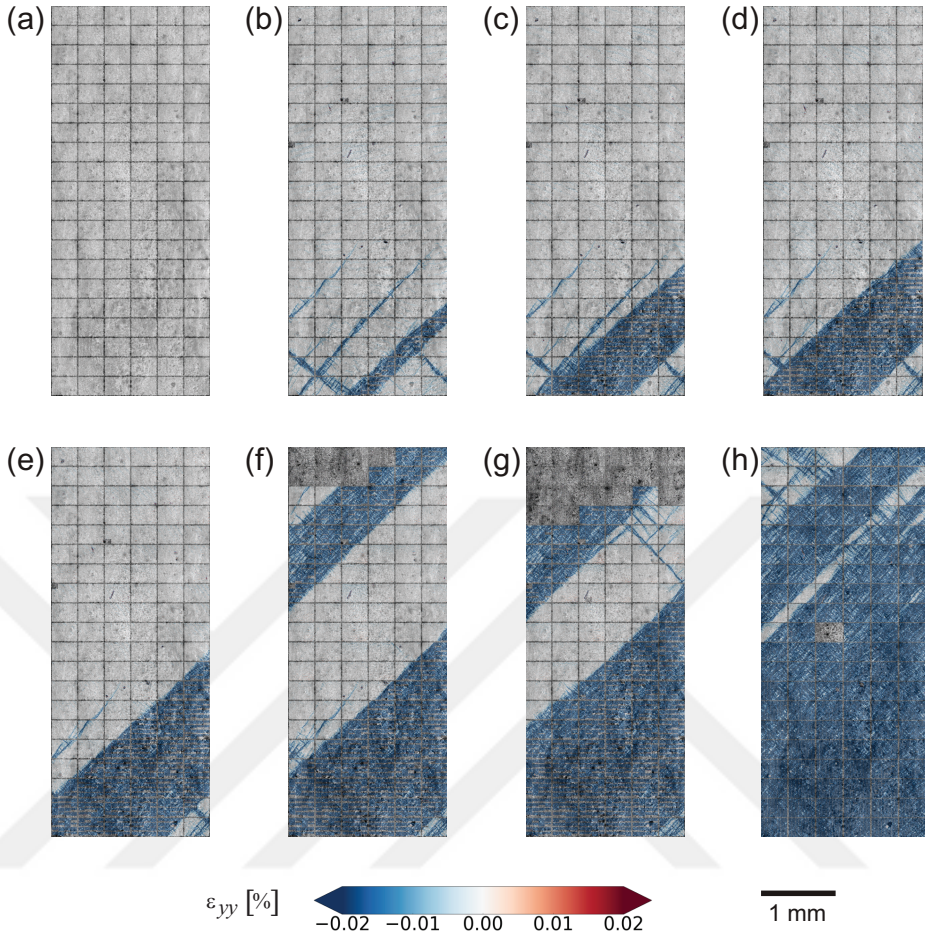

Figure 4.6. The combination plots for ε_{yy} obtained for points a to h.

They are a cross-section of the volumetric shear bands that span the entire thickness. The deformation pattern observed in this stage can be described as a 2-D plane strain deformation (recall $\varepsilon_{zz} = 0$) extruded in the third (z) dimension.

To investigate the structure of the shear bands at microscale, Figure 4.9 gives the ε_{yy} and ω_{xy} maps for the grid (8,2) at point e and h with micro-DIC resolution. Strain histograms for ε_{yy} at both load points are plotted together and provided next to the strain and rotation maps. Accordingly, grid (8,2) is mostly undeformed until load point h. At point h, two major $+45^{\circ}$ shear bands arrived at the region of this frame and their strain localization patterns are clearly seen on the strain and rotation maps. Consequently, the shape of the ε_{yy} histogram changed abruptly from the narrow *Gaussian* centered at $\varepsilon_{yy} = 0\%$ (blue curve) to a distorted distribution with a second intensity probability peak (green curve).

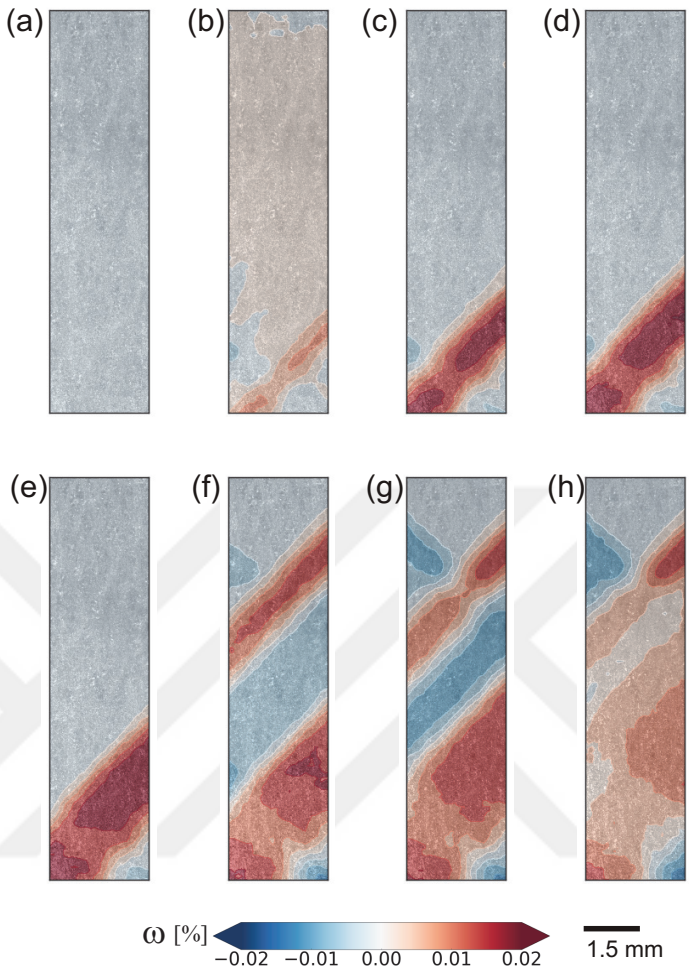

Figure 4.7. Macro-DIC results for ω fields for the top surface for points a to h.

The presence of the second peak implies two distinct statistical populations: points in the shear band and points that belong to the dormant regions. This heterogeneous and abrupt deformation pattern is observed in all of the frames. Figure 4.10 provides ω_{xy} maps for several other frames at points e and h with ε_{yy} histograms next to them. Similar to the grid (8,2), the frames shown in Figure 4.10 remain undeformed until a macroscale shear band hits the locality. Correspondingly, the shape of the histograms are changed abruptly by the generation of a *second peak*. In grid (7,6), particularly, the second peak consumes the initial peak completely, since there is no dormant region left in this frame.

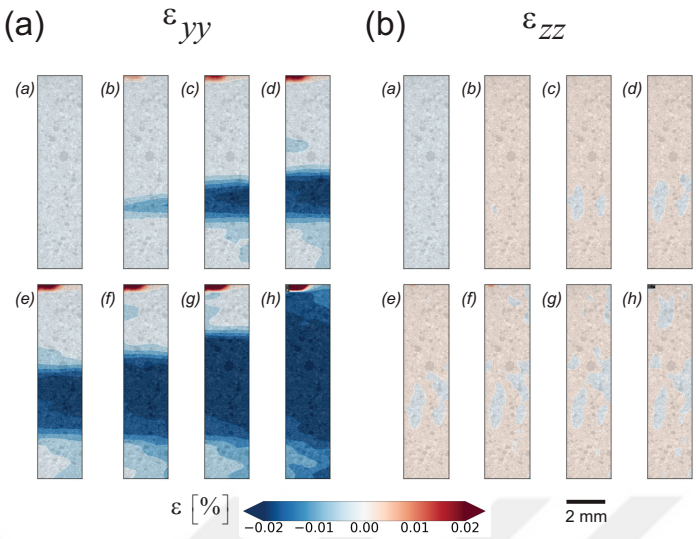

Figure 4.8. Macro-DIC results for (a) ε_{yy} and (b) ε_{zz} fields for the side surface for points a to h.

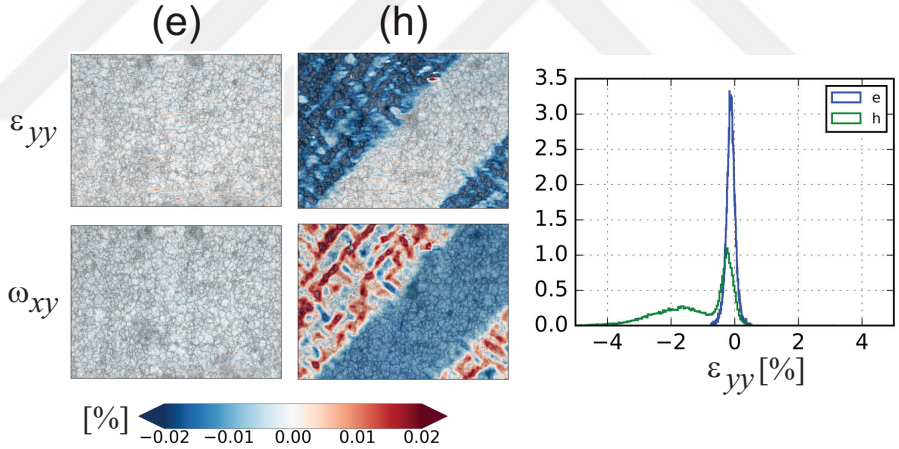

Figure 4.9. ω_{xy} and ε_{yy} maps and the ε_{yy} histogram for frame (8,2) obtained for load points e and h.

The heavy strain localization pattern at the sample scale and the *abrupt* development of strain heterogeneity at the microscale directly point to a spatially coordinated activity of deformation micromechanism(s). Considering the limited options of straining mechanisms in Mg AZ31 and the abrupt nature of deformation discussed above, $\{10\bar{1}2\}\langle\bar{1}011\rangle$ tensile twin system is concluded to be the micromechanism that drives the observed deformation behavior. The very fact that TP1 (first twin plateau) is dominated by tensile twin activity clearly supports this conclusion.

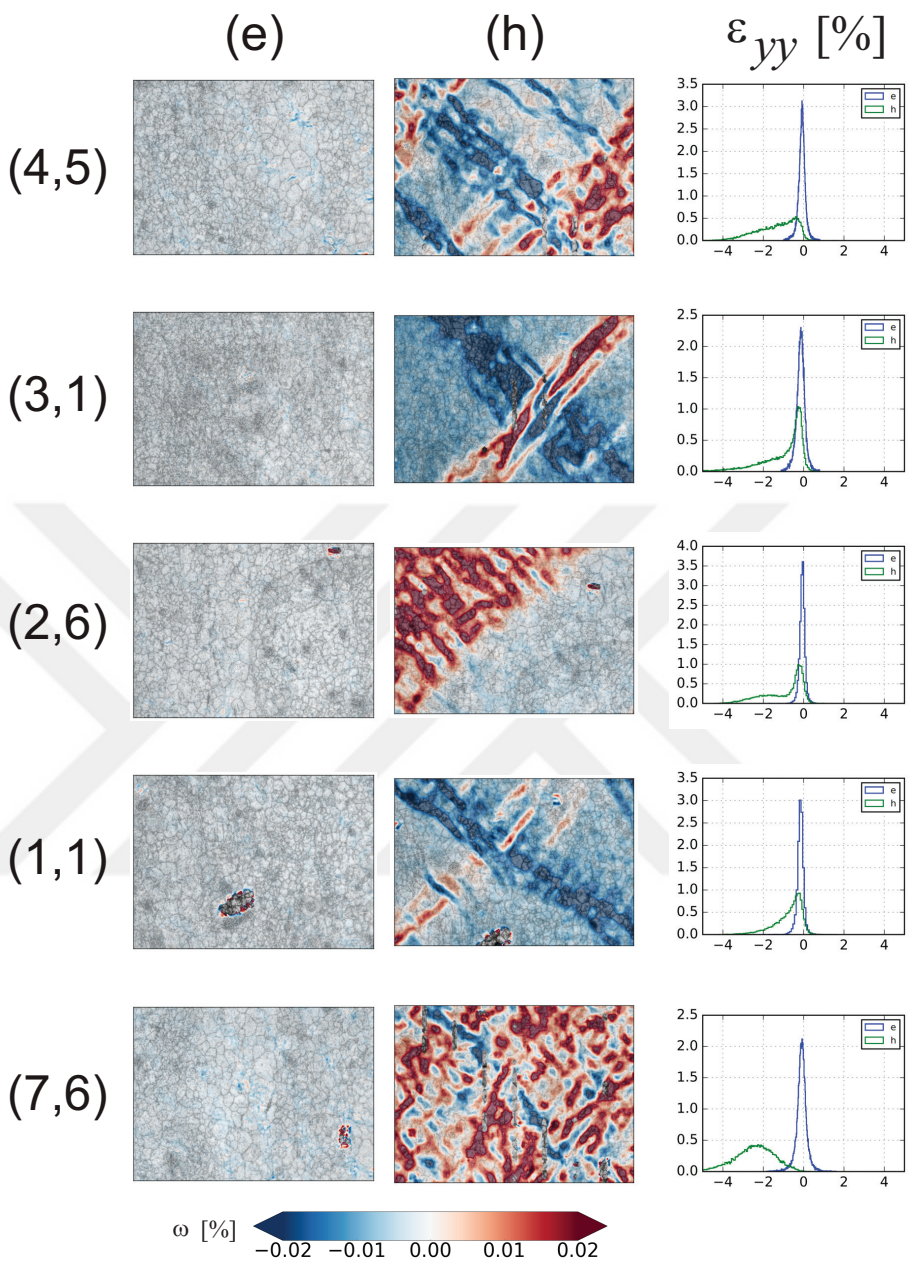

Figure 4.10. ω_{xy} maps and ε_{yy} histograms for the selected frames obtained for load points e and h.

To illustrate this point, Figure 4.11a and Figure 4.11b depicts the two limiting preferred orientations inside the sample. Tensile twin processes on the shown twin planes of the preferentially oriented grains produce $\pm 43.3°$ and $\pm 50.8°$ shear bands on the TD surface respectively which are closely aligned with the observed $\pm 45°$ shear band patterns.

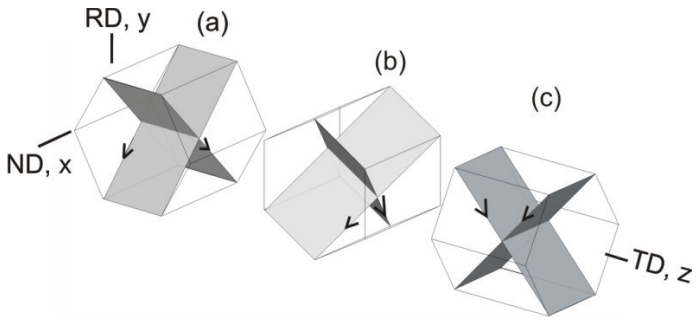

Figure 4.11. The orientations of twin planes and twinning directions for the tensile twin mechanism in rolling texture for the equally possible texture orientations (a) $\langle 11\bar{2}0\rangle$//TD and (b) $\langle 10\bar{1}0\rangle$//TD. (c) The unpreferred crystal orientation $\langle 0001\rangle$//TD.

Therefore, the macroscopic shear banding stems from the coordinated activity of tensile twin mechanism (with any accompanying necessary slip activity) over the grain networks inside the shear bands. These findings over the first twin plateau reproduce the conclusions of Aydıner and Telemez [34] whose monotonic loading span only covered the twin plateau.

4.2.2. Reversal from compression - detwinning step

The sample is unloaded at point h ($\varepsilon_M = -1.97\%$) and then reverse-loaded in tension heading into the detwinning ramp (DR) in Figure 4.1. Micro-DIC points selected in the DR region are specifically shown on the stress-strain curve in Figure 4.12. Unload from point h and mild reverse-load up to point i (Figure 4.12) deviates slightly from linearity which indicates limited reverse plasticity with predominantly elastic behavior. Substantial detwinning occurs only after this point signified with a substantial change in the slope of the stress-strain curve. ω_{xy} and ε_{yy} combination maps obtained at micro-DIC points are given in Figure 4.13 and Figure 4.14 respectively.

ω_{xy} and ε_{yy} maps (Figure 4.13 and Figure 4.14) show the recovery of the $\pm 45^\circ$ band patterns in the DR region.

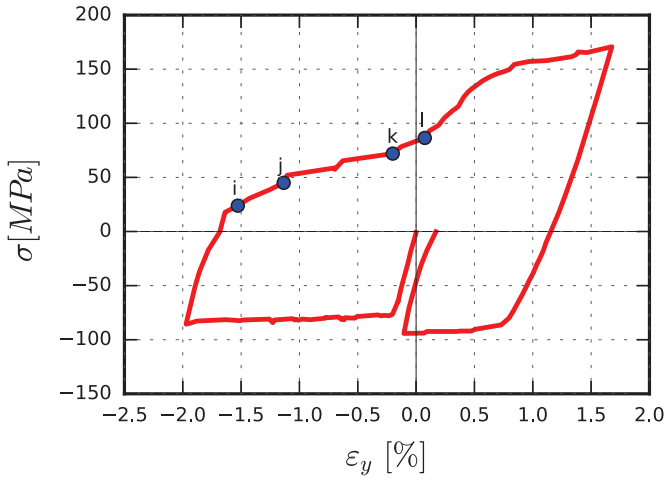

Figure 4.12. Micro-DIC analysis points $i,\ j,\ k$, and l are designated in the DR region.

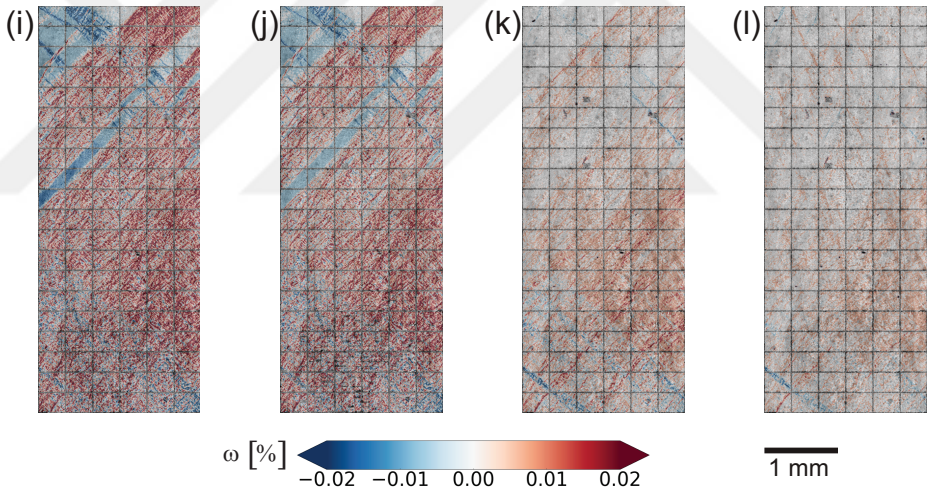

Figure 4.13. The ω_{xy} combination plots obtained for points i to l.

The strain intensity of the shear bands decrease in response to the imposed tensile strain increments. The deformation recovery in DR, as in the case of TP1, happens in discrete sudden steps. Recall shear bands formed and expanded abruptly in TP1, and deformation progressed by the nucleation of a band or the arrival of a band. Similarly, in the DR region, strain decrements occur with *recovery bursts* over the shear bands. This leads to the serrations on the DR portion of the stress-strain curve. In each serration, the stress jumps by about $8 - 10$ MPa. The recovery bursts are, however, different from the TP1 shear banding in a spatial sense:

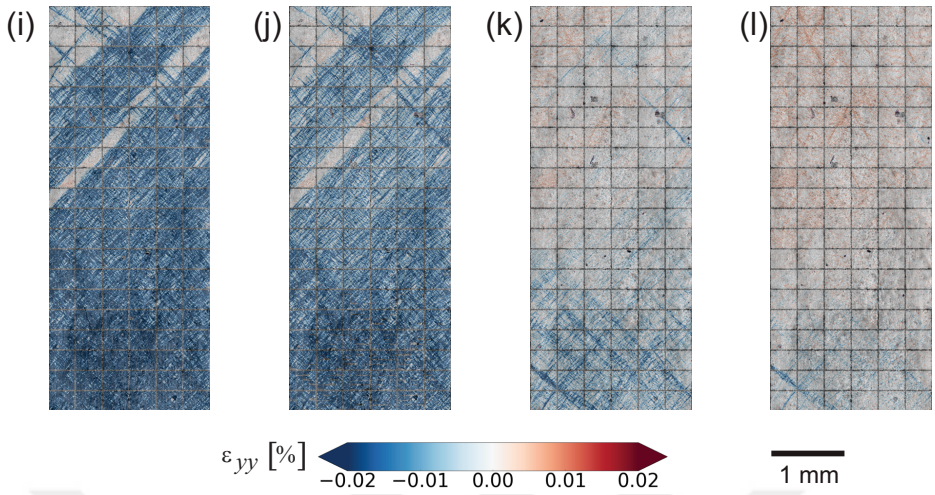

Figure 4.14. The ε_{yy} combination plots obtained for points i to l.

Recovery in DR occurs homogeneously over all shear band structures rather than a *cascaded* shrinkage of individual regions. This is most clearly seen by comparing Figure 4.13j to Figure 4.13k, where the two major $+45^{\circ}$ shear bands are recovered at the same time, in contrast to the sequential formation observed in TP1.

By load point l, the compressive strain content is mostly recovered and the transition region (HHR) is impending. It should be emphasized that the transformation strain imposed on the structure in the TP1 region is near fully recovered in the DR region. However, a noticeable spatial variation exists roughly between the bottom and top regions of the gage section. This spatial heterogeneity does not stem from the detwinning process itself but actually a remnant of the strain heterogeneity at the reversal point of TP1, point h. Though the strain bands covered nearly the entire surface at this point, the bottom section of the sample undergoes higher shear band activity and accommodates more strain. Naturally, even with roughly homogeneous recovery in DR, the bottom of the sample lags behind and the strain states remain compressive compared to the top. This is why even at the overall strain becomes slightly tensile at point l ($\varepsilon_M = 0.075\%$), the recovery processes at the bottom side of the sample are persisting. On the other hand, the top part of the sample has recovered completely and strain localization patterns with tensile character (Section 4.2.3) have already started to form in this region (positive ε_{yy} (red) high angle bands visible in Fig 4.14l).

This picture indicates a progressive *spatial transition* between DR and HHR stages as more of the sample finishes twin recovery and is forced to incur tensile strain increments with other forms of plasticity.

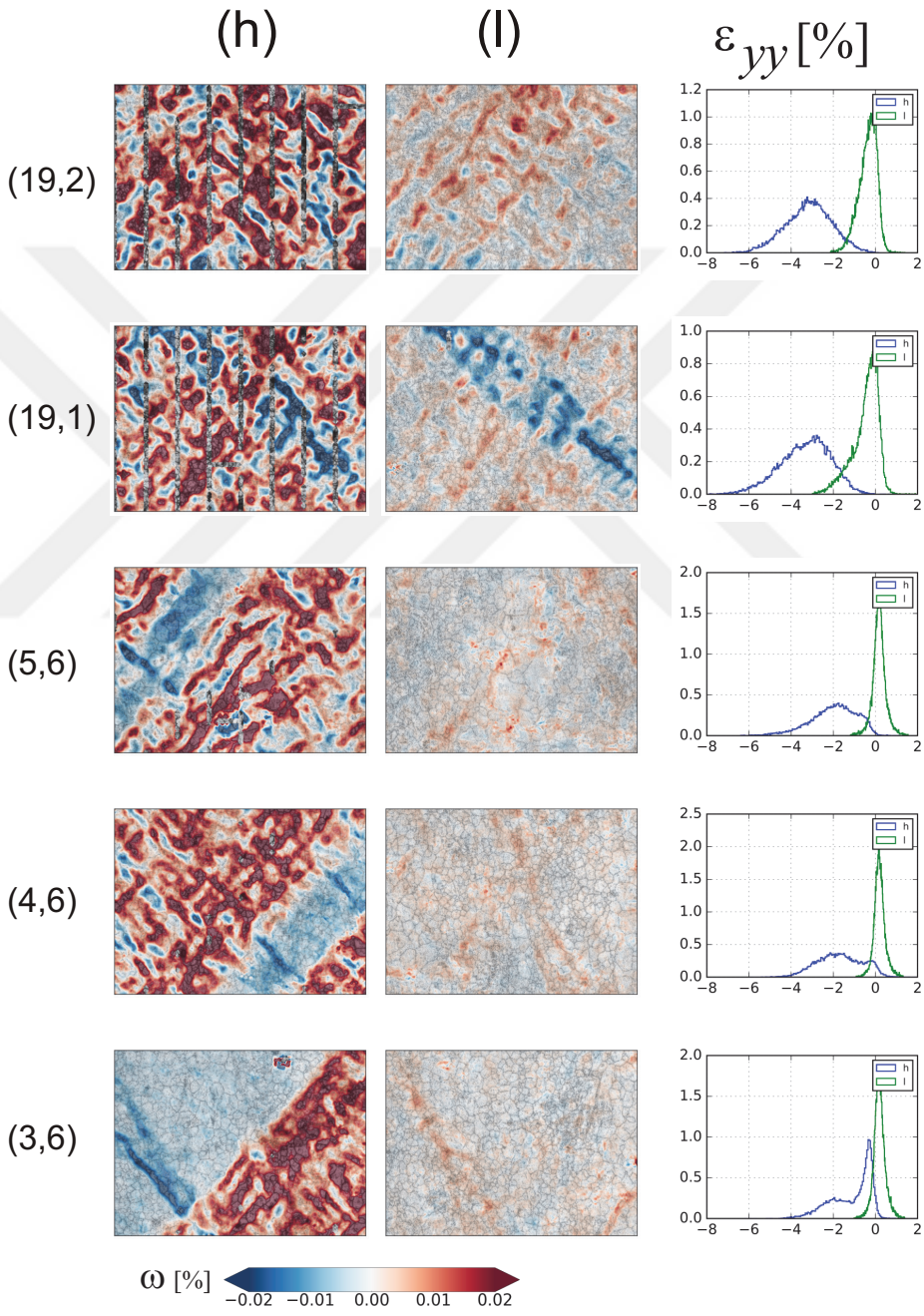

Figure 4.15. The ω_{xy} maps and ε_{yy} histograms for the selected grids obtained for load points h and l.

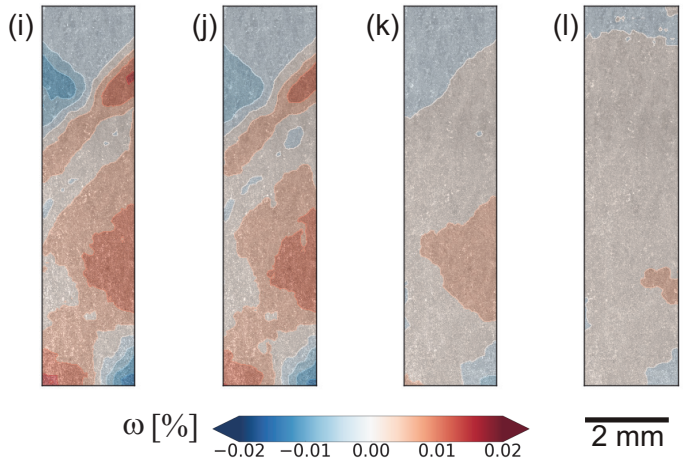

Figure 4.16. The top surface macro-DIC ω_{xy} maps obtained for load points i to l.

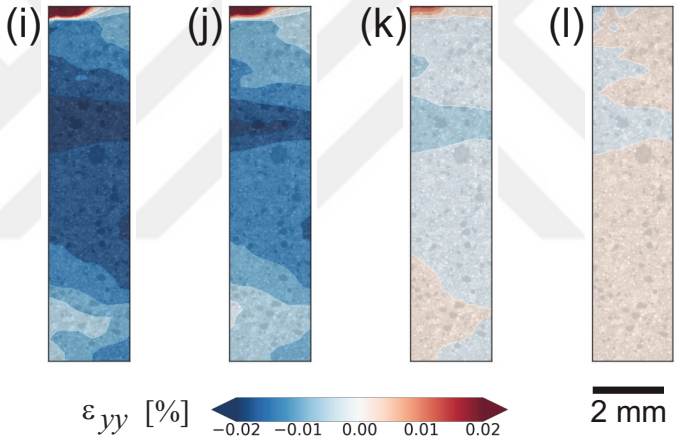

Figure 4.17. The side surface macro-DIC ε_{yy} maps obtained for load points i to l.

Strain recovery in DR, as was the case for the emergence of the TP1 shear bands, is volumetric. The macro-top ε_{yy} maps and the macro-side ε_{zz} maps for load points *i, j, k* and l are given in Figs.4.16 and 4.17. As the shear bands recovered between load points i to l, shear band patterns resolved at the macroscale shrink concurrently. Strain intensity inside the horizontal band on the side surface and cross-bands on the top surface decrease with the tensile strain increments from point i to l.

For the microscale analysis of the transformation strain recovery, ω_{xy} maps and ε_{yy} histograms of frames (19,2), (19,1), (5,6), (4,6), and (3,6) are considered in Figure 4.15). From points h to l, deformation patterns are recovered in each frame.

From a mechanistic point of view, notice that the deformation recovery process in the DT stage is the opposite of the deformation process in the TP1 stage. That is, second peaks formed during deformation in the TP1 stage are now consumed by a *gaussian* peak centered at 0% strain. This is clearly seen in grid (3,6) (Figure 4.15), where the strain histogram for the frame at point h (blue curve) have a second peak pointing to the strain content of the $+45^{\circ}$ shear band. The second peak is consumed by the central dormant peak (green curve) by point l. Although deformation recovery is not fully completed, the shapes of the histograms at point l signifies significantly reduced deformation heterogeneity. For grids (19,1) and (19,2) recovery is not complete at point l and some traces of the bands remain. For the other grids deformation is mostly recovered though. This difference between grids is visible from the histograms too, since the strain histograms at point l for grids (19,1) and (19,2) are relatively broader than those for grids (5,6), (4,6) and (3,6).

Both macroscale and microscale analyses verify that the compressive transformation strain imposed in TP1 is *reversed* during DR. Notice macroscopic strain could be zero even when microscopic strains of the same region have a large spread with tensile and compressive strains that average out. Here, microscale recovery occured without any significant remnant plasticity. Such deformation behavior seems to be explicable only with the predominant activity of $\{10\bar{1}2\}\langle\bar{1}011\rangle$ twinning-detwinning mechanism throughout TP1-DR regions.

4.2.3. Transition region - High hardening ramp

The slope of the stress-strain curve sharply rises at the end of the DR region about point l in Figure 4.18, and the form of the stress-strain curve is changed from a relatively flat plateau to a high hardening ramp. The material is hardened by 61 MPa in the high hardening ramp (HHR) from the near-zero-strain point l to point p at $\varepsilon_M = 0.97\%$. Micro-DIC points $l,\ m,\ n$ and o are on the HHR region. The ω_{xy} and ε_{yy} maps at these micro-DIC points are given in Figs. 4.19 and 4.20, respectively.

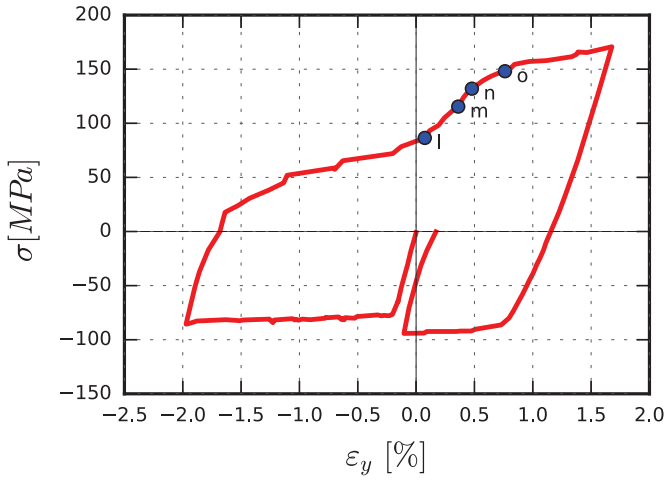

Figure 4.18. Micro-DIC analysis points l, m, n, and o are designated in the HHR region.

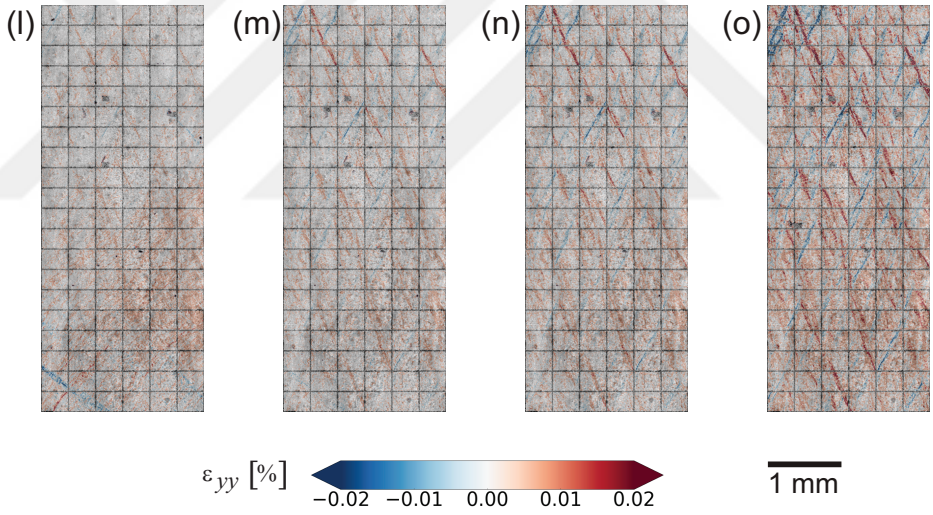

Figure 4.19. The ω_{xy} combination plots obtained for points l to o.

As mentioned in the detwinning section (Section 4.2.2), the transition from detwinning mode to high hardening mode carries the macroscopic strain heterogeneity inherited from TP1. Consistenly in HHR, detwinning processes are observed to continue on the bottom side of the sample even up to load point n. All the compressive deformation patterns ($\pm 45°$) are recovered and the tensile deformation patterns are distributed over the TD surface by this point as seen in Figs. 4.19n and 4.20n. The tensile deformation patterns (or, to say, strain localizations) nucleate as lenticular structures and then elongate with further strain increments.

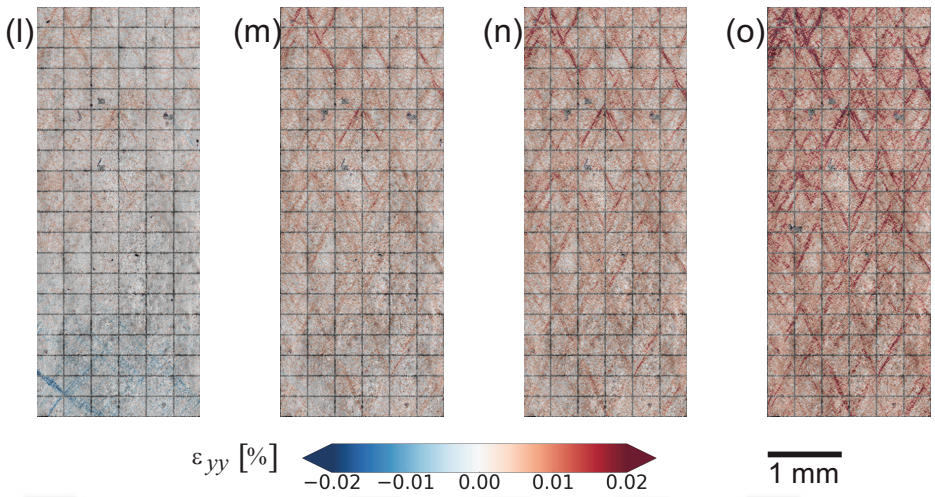

Figure 4.20. The ε_{yy} combination plots obtained for points l to o.

The orientations of these bands stray approximately 15° from the $\pm 45^\circ$ maximum shear planes towards the loading axis. These structures will be referred to as *high angle bands* for the rest of the thesis.

The high angle bands are considerably thinner (more localized) compared to the $\pm 45^\circ$ shear bands of the TP1 region. However, their distribution is more homogeneous, i.e, the HHR region consists of many high angle bands distributed over the TD surface. This is dissimilar to the shear banding behavior observed in TP1, where local bands coordinate to sample-scale $\pm 45^\circ$ bands. In a temporal sense, the formation and expansion of the high angle bands is gradual, contrary to the sudden and abrupt development of the TP1 shear bands. Any pronounced serration is absent on the HHR region of the stress-strain curve.

The inclination angle of the high angle bands with respect to the loading axis seems to be characteristic. Nominally, the bands appear slanted at approximately $\pm 60^\circ$ that is 15° away from the maximum shear planes. Any macroscopic shear band structure (if it forms) in a roughly isotropic polycrystalline material is expected to be aligned with the maximum shear planes. However, the heavy basal texture of the present sample apparently enforces a pronounced anisotropic behavior where only certain deformation micromechanism(s) whose plane of shear is closely aligned with the high angle bands are available to yield tensile plastic strain.

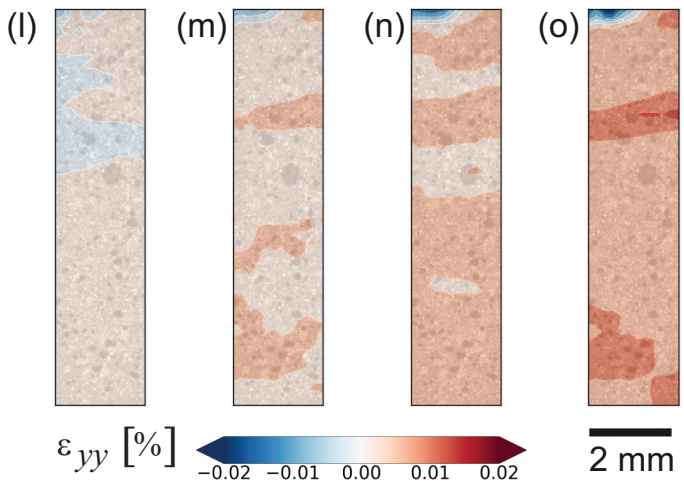

Figure 4.21. The side surface macro-DIC ε_{yy} maps obtained for points l to o.

The deformation patterns of the high angle bands are not resolved with macro-DIC resolution. The length scale of the high angle bands remain too low compared to the subset size used for the macro-DIC analysis. The top surface macro-DIC maps (omitted for brevity) only present the aforementioned strain distribution differences between top and bottom regions. On the other hand, side surface maps point to some other strain localization patterns. Side surface ε_{yy} maps for points l to o are provided in Figure 4.21. The strain map for point l (Figure 4.21l) indicates a light blue band (mild compressive strain) located on the top side of the sample which does not undergo complete strain recovery during the detwinning process (Figure 4.17 in Section 4.2.2). Later at point o (Figure 4.21o), the region of this band now exhibits tensile strain localization. So, interestingly the band that was lagging behind in strain, suddenly rushes to accommodate more tensile strain than the rest of the structure. This strain band further grows in the upcoming tensile plateau region that follows HHR.

Micro-DIC analysis of the individual frames reveals the strain heterogeneity inflicted by the formation of the high angle bands. Figure 4.22 provides the ω_{xy} maps and the ε_{yy} histograms of frames (9,2),(4,6),(3,6) and (2,2) at point l and o. At point l, that roughly marks the end of DR, these frames are virtually free of prior deformation. Accordingly, the strain histograms at point l (blue curves) are centered around 0 strain with a Gaussian shape. The histograms are relatively narrow signifying a homogeneous distribution. With the advance of further strain increments, high angle bands appear in each frame.

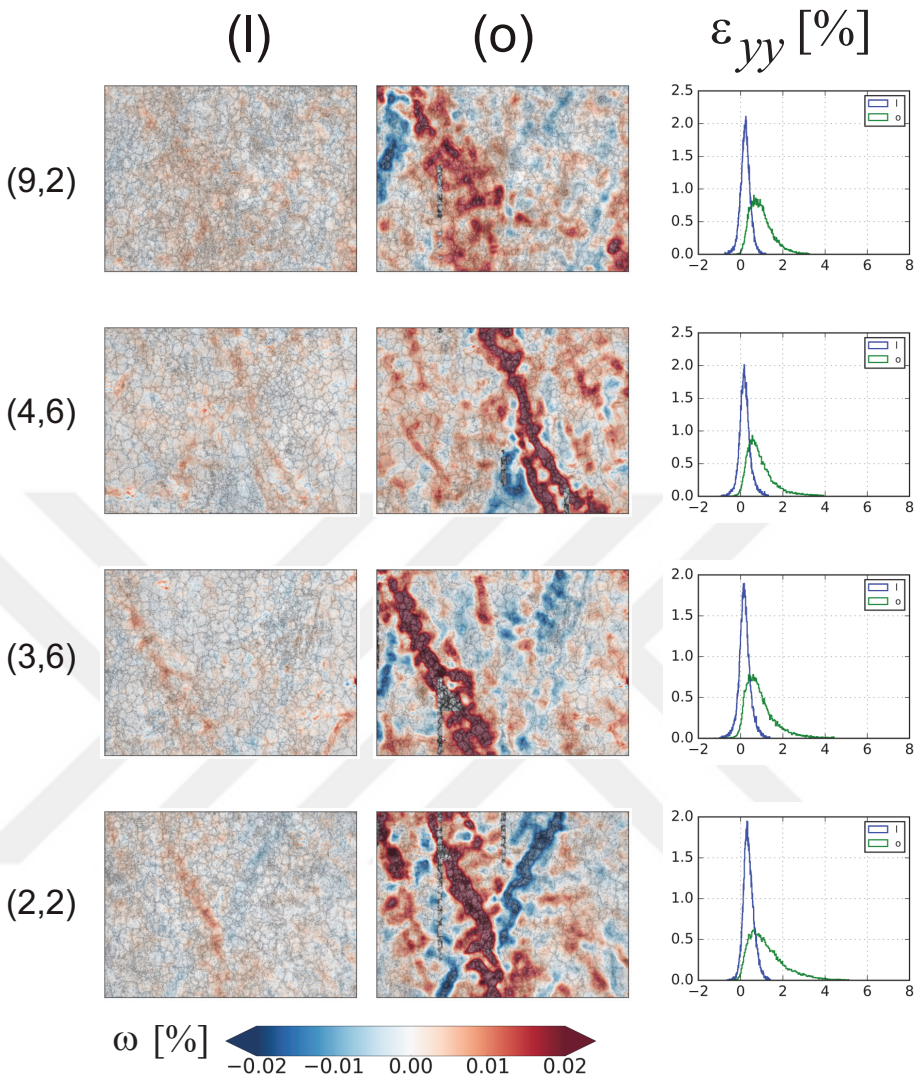

Figure 4.22. The ω_{xy} maps and ε_{yy} histograms for the selected frames obtained at points l and o.

The formation of these shear bands manifest as a broadening of the strain histograms (green curves in Figure 4.22). The level of strain heterogeneity rose significantly, with the strain distribution ranging from 0 to 4% strain. Along with the broadening of the histograms, they shift towards the positive strain side as a whole (The proper average of the histograms naturally should yield the average strain).

The mechanism responsible for the formation of the high angle bands is yet to be identified. Reverse and/or cyclic loading tests conducted by other researchers claim that dislocation slip plays the predominant role for compression along the c-axis [5, 18, 19, 26].

(Recall, due to Poisson effect, tension along loading axis RD implies compression along the c-axis for the orientations that the initial texture favors.) Proust et al. (2009) [18] conducted extensive monotonic and reverse loading tests to investigate the anisotropic deformation behavior in Mg AZ31 sheet material with a typical basal texture. They also formulated a crystal plasticity scheme that accounts for the hardening behavior from interaction between the slip and twinning systems. They found that compression along the c-axis was mainly accommodated by $\langle a \rangle$ basal, $\langle a \rangle$ prismatic and $\langle c + a \rangle$ pyramidal slip systems. Wu et al. (2015) [19] conducted a neutron diffraction study on Mg AZ31 where a sample cut from a rolled plate was loaded such that twinning-detwinning was extensively activated. This study covered the main characteristics of low-cycle fatigue tests under 2% strain amplitude, and mainly focused on the texture evolution. They attribute the cyclic hardening behavior to residual twin content and dislocation slip activity whose effect increases with cycle number. Guillemer et al. (2011) [26] investigated the monotonic and cyclic loading behavior of pure extruded magnesium along the extrusion axis (imposing a compression along the c-axes as in the present study), and suggested that the material responded with hard slip systems like $\langle a \rangle$ prismatic and $\langle a \rangle$ pyramidal and $\langle c + a \rangle$ pyramidal systems. Lou et al. (2007) [5], also attributes the high hardening behavior on the tension side of loading a sheet Mg AZ31 sample to slip activity without distinguishing any specific system. All of the above studies rule out $\{10\bar{1}1\}\langle 10\bar{1}2 \rangle$ compression twinning as a predominant mechanism. However, none of the above studies account for the strain localization and deformation heterogeneity observed in this study and their conclusions are based mainly on crystal plasticity simulations. The formation of the high angle bands suggests a very structured interplay between the cited micromechanisms for this sharp texture. Further discussion about the character of the high angle bands and the probably underlying mechanisms is in Section 4.2.8.1.

4.2.4. Tensile Plateau

The tensile plateau onsets at $\sim$ 153 MPa in Figure 4.18. The significant difference between onset stress levels of the first twin plateau (TP1) and the tensile plateau (TensPlat) (-82 MPa and 153 MPa respectively) depicts the extreme tension-compression anisotropy exhibited by this material.

Though the substantial hardening in the HHR region diminishes in the TensPlat, there is still noticeable hardening in the tensile plateau, more so than the nearly perfectly-plastic TP1. The plastic strain accommodation is gradual and lacks the serrations of TP1 that are linked with abrupt shear banding. Micro-DIC analysis is conducted at points $p,\ q$, and r which are shown on the stress-strain curve of Figure 4.18.

The combination plots for ω_{xy} and ε_{yy} at the micro-DIC points are given in Figs. 4.19 and 4.20, respectively. Plastic deformation is concentrated around the high angle bands, however, the strain localization patterns are significantly more diffuse (homogeneous) compared to the patterns observed in TP1. The high angle bands that had a thin and lenticular shape in the HHR region expand in TensPlat with further accumulation of plastic deformation around them. It stands to reason that the HHR bands served as stress concentration sites about which harder deformation mechanisms could be more easily activated as the material switches to large scale plasticity.

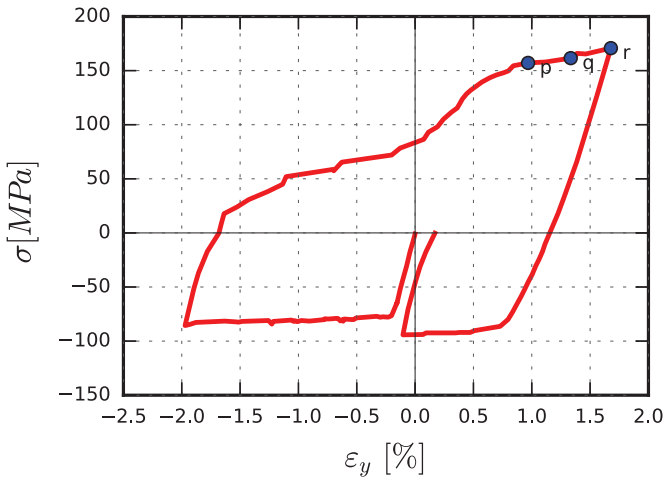

Figure 4.23. Micro-DIC analysis points $p,\ q$, and r are designated in the TensPlat region.

The horizontal streak that formed on the side surface in HHR mildly expands and strain intensity increases in TensPlat, clearly discerned on the side surface ε_{yy} maps in Figure 4.26. The horizontal band is designated between two yellow dashes in Figure 4.26r. In addition to this band, another strain localization pattern is resolved on the bottom side of the side surface.

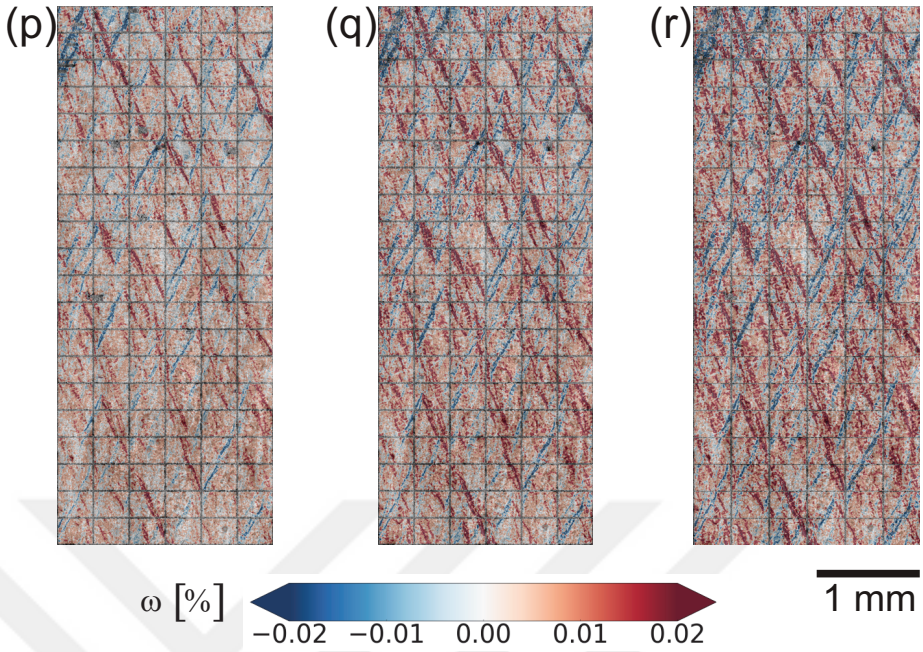

Figure 4.24. The ω_{xy} combination plots obtained for points p to r.

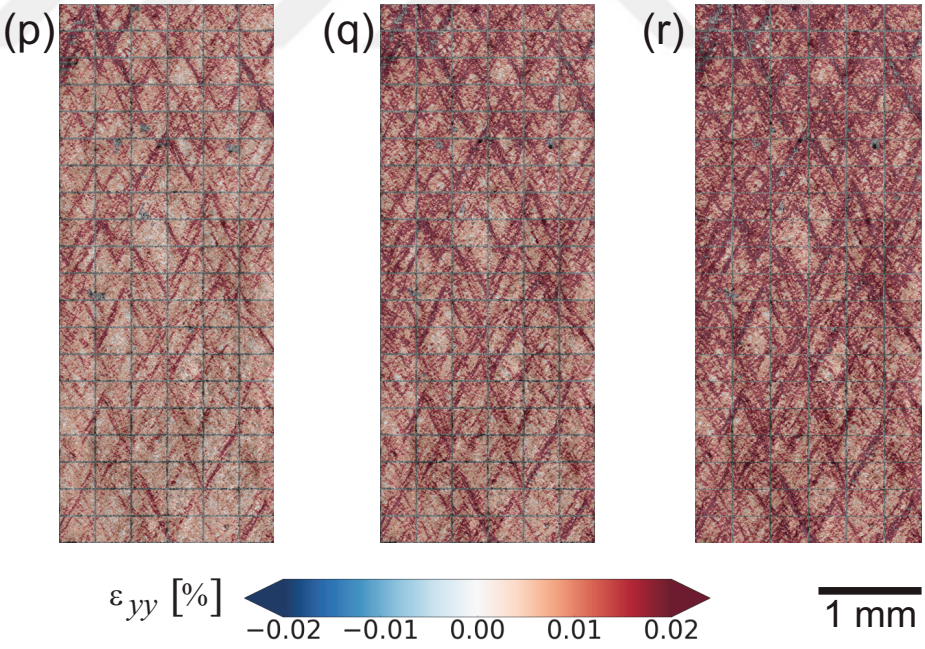

Figure 4.25. The ε_{yy} combination plots obtained for points p to r.

The site of the second localization corresponds to an incomplete recovery region at the end of DR, as was the case for the first horizontal streak on the side surface. Recall that the traces of the bottom $+45°$ band survived even until load point l (Section 4.2.3, Figure 4.20l).

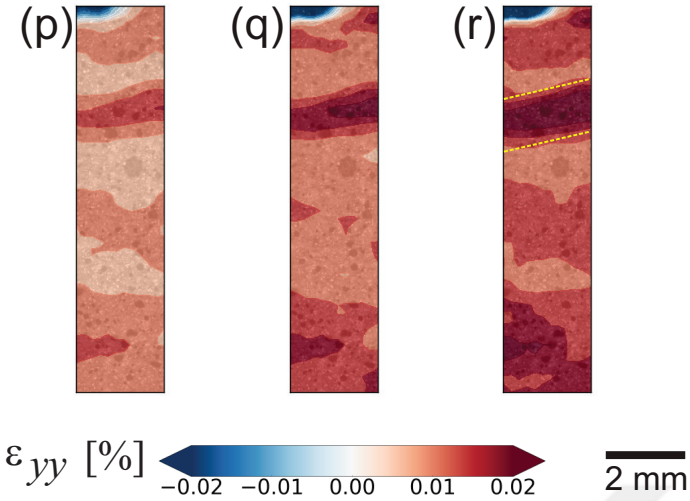

Figure 4.26. The side surface macro-DIC ε_{yy} maps obtained for points p to r.

Such an observation suggests that the formation of high angle bands and consequential localization around them are correlated with the remnant (unrecovered) plasticity from the TP1 pattern.

The increase in the deformation heterogeneity in the TensPlat region is revealed at the microscale in a similar manner to the HHR region. Figure 4.27 provides the ω_{xy} maps and ε_{yy} histograms of some selected frames for points o and r. These regions already accommodated some high angle band structures at point o which lead to the fairly broad strain histograms (blue curves). Deformation patterns, then, grow and cover the entire frame by point r. Correspondingly, the range of the strain histograms stretch to a maximum strain of $\sim 6\%$ (green curves). From point o to r, the frame-averaged ε_{yy} strain increases from $\sim 0.8\%$ to $1.5 - 1.8\%$. The resulting shape of the strain histograms are roughly *Gaussian*, unlike the two-peak strain histograms observed in the TP1 region. Spatially, this refers to a relatively homogeneous deformation over the regions of each frame (of course with some localization bound to occur in a polycrystalline aggregate) in HHR and TensPlat, unlike the strain fields that featured distinct regions of deformed and dormant material points in TP1.

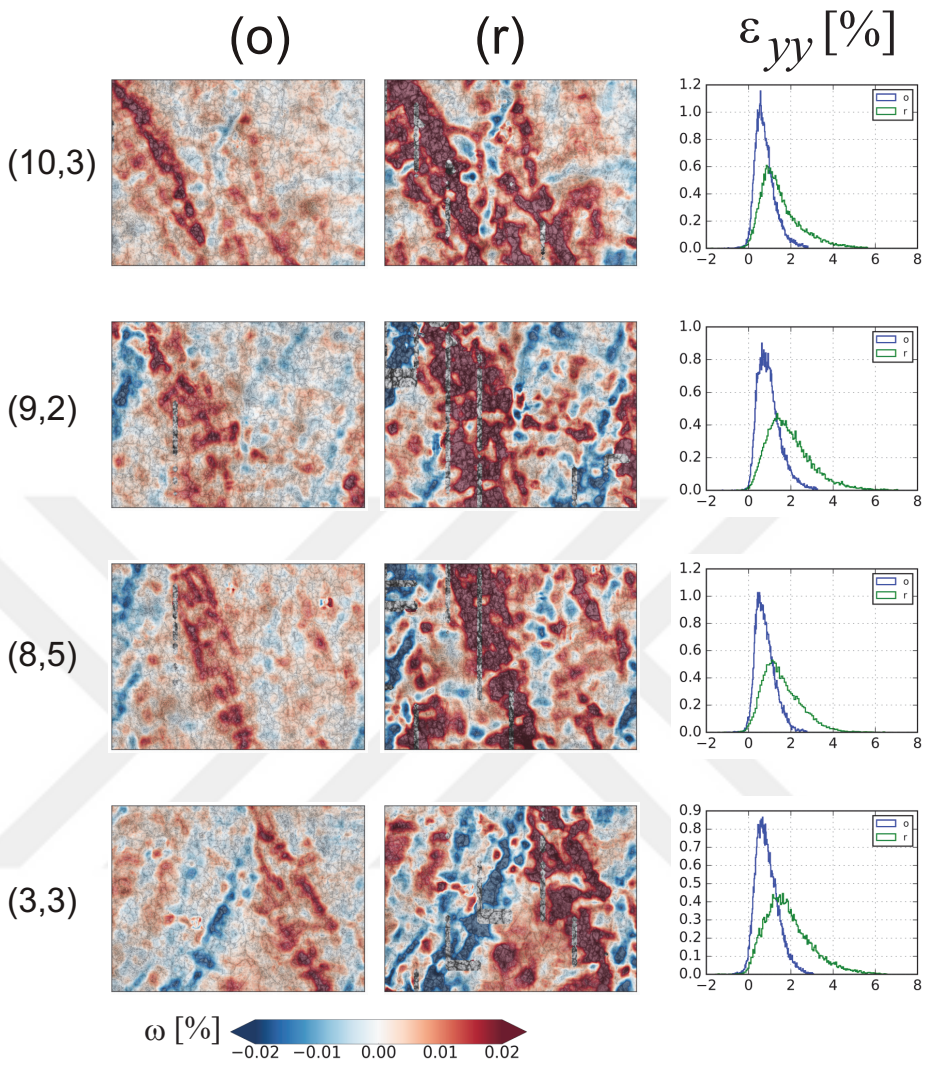

Figure 4.27. The ω_{xy} maps and ε_{yy} histograms for the selected frames obtained for load points o and r.

The high angle bands increase surface roughness significantly. Although this was not apparent from the top surface macro-DIC strain maps, possibly due to DIC subset averaging, their marks on the surface were easily discerned in the bare macroscopic images. Figure 4.28 shows the evolution of the traces of the high angle bands, that appear as thin white lines. These pronounced traces indicate significant roughening of the surface since in the reflective microscopy mode, the alteration of the image intensity is strongly associated with the disturbance of the surface topography.

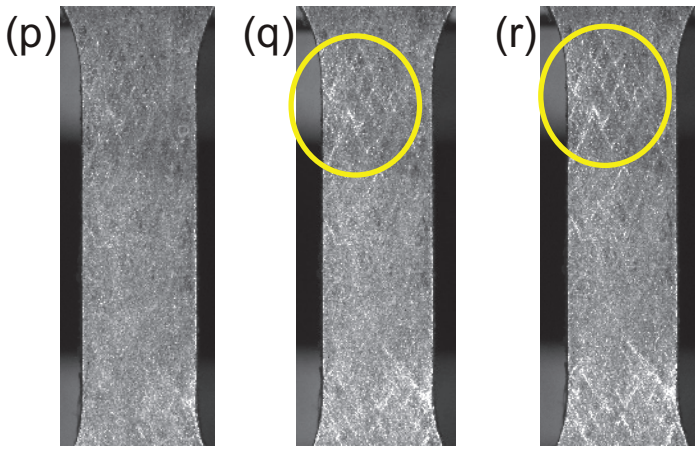

Figure 4.28. Direct observation of high angle shear band patterns due to increasing surface roughness of the top surface from point p to r at macro-DIC resolution.

4.2.5. Reversal from tension

The loading direction is reversed again at load point r ($\varepsilon_M = 1.6\%$). Selected points at which micro-DIC analysis is conducted are shown on the stress-strain curve in Figure 4.29. Since the unloading is mostly elastic, microscale DIC analysis is performed at only two load points. At load point s, the sample is fully unloaded, and the nominal strain went down from a $\varepsilon_M = 1.6\%$ to $\varepsilon_M = 1.15\%$. The loading is reversed for the second time following this point, this time in compression. The next point t is hence on the compressive side of the stress line ($\sigma = -69$ MPa). The stress-strain curve leading to this point still shows linear trend.

Figures 4.30 and 4.31 present the full-field ω_{xy} and ε_{yy} maps measured at points s and t. The ω_{xy} maps show that the high angle shear bands formed and developed in the HHR and TensPlat regions are preserved during the reverse loading. The ε_{yy} maps, though preserving the remnant strain localization structures, show a homogeneous decrease in the strain content. This appears as a homogeneous reduction in the color intensity over the entire strain map.

The microscale analysis results also clearly point to merely elastic unloading and reverse loading of the sample until point t.

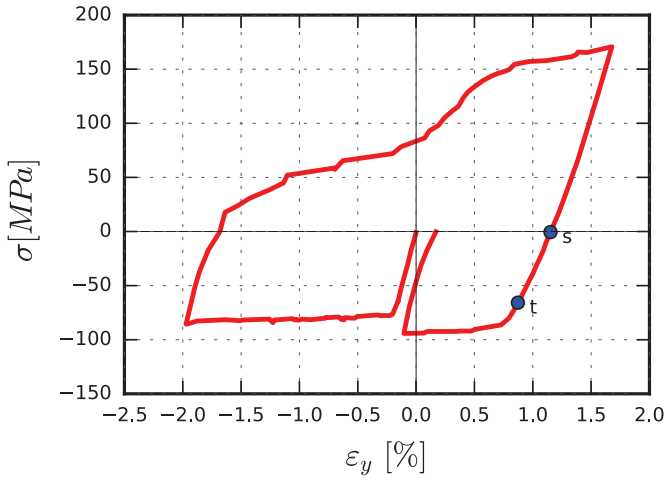

Figure 4.29. Micro-DIC analysis points s and t designated in the RevTens region.

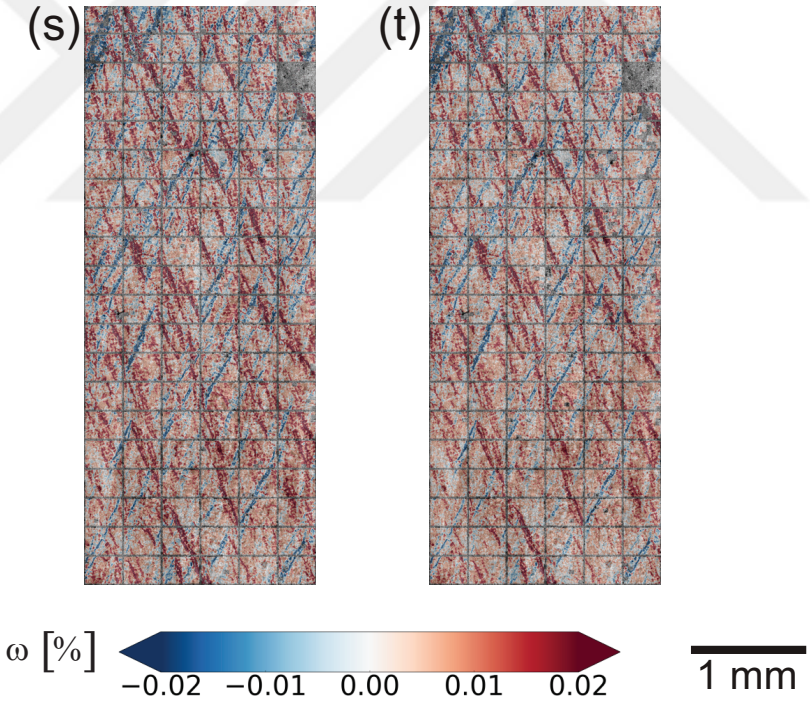

Figure 4.30. The ω_{xy} combination plots obtained for points s and t.

The band patterns at point r that are present in the grid (9,2) and (3,3) regions still prevail at point t as shown by the ω_{xy} maps given in Figure 4.32. The strain histograms shift towards the 0 strain axis without changing their shape.

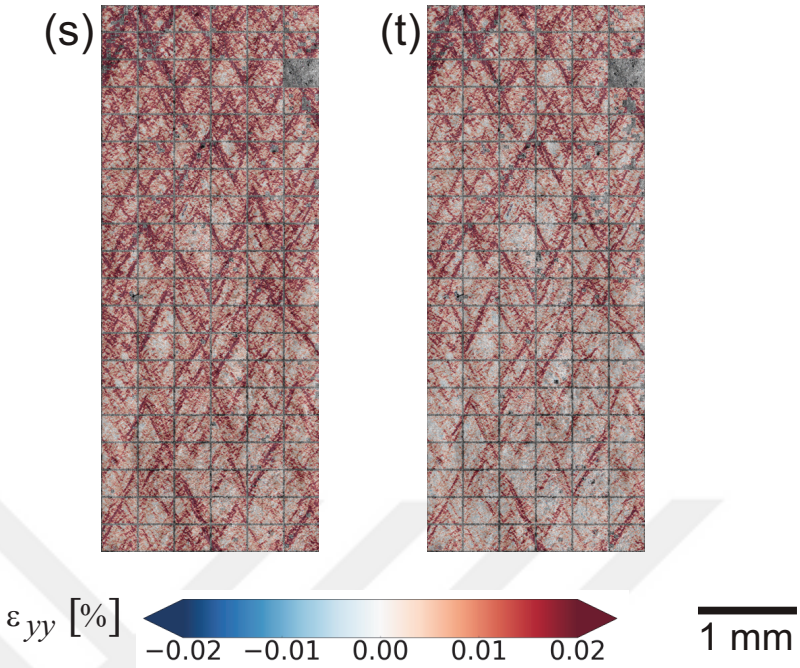

Figure 4.31. The ε_{yy} combination plots obtained for points s and t.

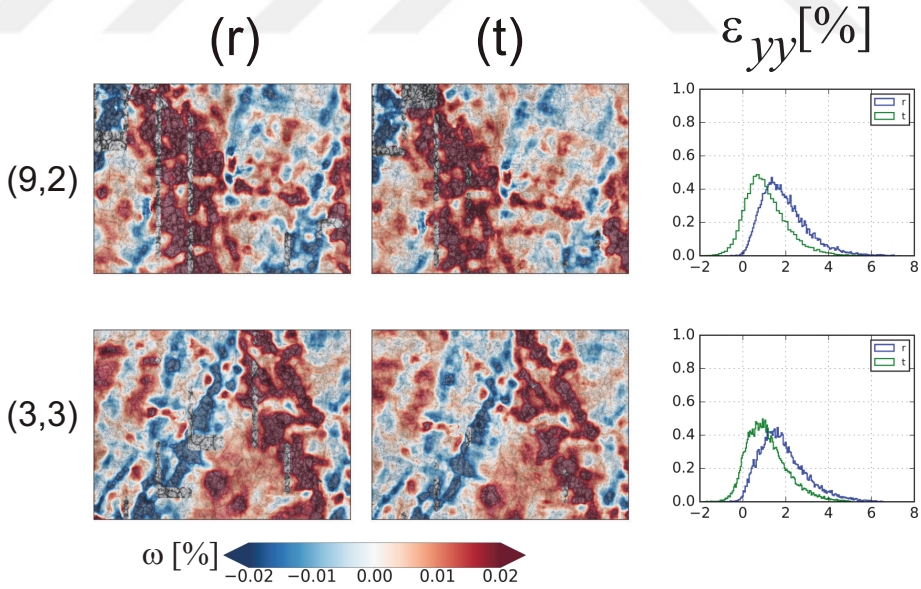

Figure 4.32. The ω_{xy} maps and ε_{yy} histograms for the selected frames obtained for load points r and t.

This implies that all plastic strain structures that have led to the spread in these histograms have been sustained and the strain in these steps were elastic and homogeneous in character.

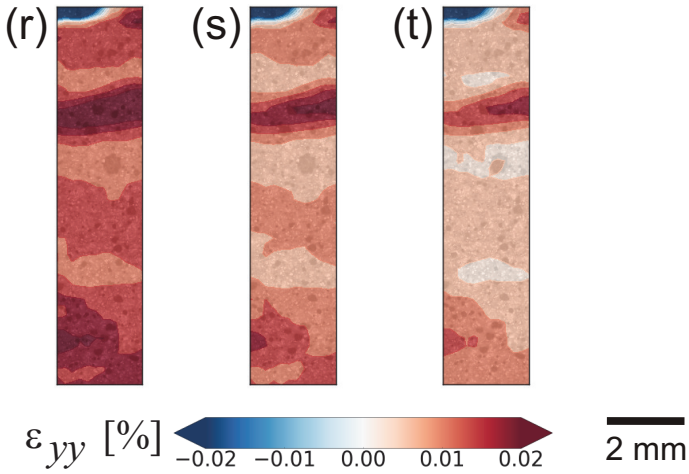

Figure 4.33. The side surface macro-DIC ε_{yy} maps obtained for points r, s and t.

The side surface ε_{yy} maps (Figure 4.33) are also consistent; pointing to a homogeneous unstraining from point r to point t.

4.2.6. Second compression stage

The second twin plateau (TP2) onsets around -89 MPa. This value points to a $\sim 8\%$ hardening over the virgin material of the first loading cycle TP1. TP2 exhibits the typical low hardening slope (Figure 4.34) which is characteristic of twinning-dominated deformation. The labelled micro-DIC points on TP2 are u, v and w. Point x follows the final unload from TP2 (the end point of the experiment). The measured full-field ω_{xy} and ε_{yy} maps are given in Figs. 4.35 and 4.36, respectively. Point u is located at the onset of the twin plateau. The deformation patterns at point u does not much differ from the patterns that are present at point t. The new $\pm 45^{\circ}$ shear band patterns associated with the second twin plateau appear at point v. With the development of these bands, two distinct families of deformation patterns coexist in the material: the high angle bands and the new family of $\pm 45^{\circ}$ bands. By point w, new $\pm 45^{\circ}$ bands nucleate and the existing ones expand to cover more than half of the micro-DIC surface. The new $\pm 45^{\circ}$ bands and the pre-existing high angle bands intermingle, especially on the top side of the micro-DIC surface. The ω_{xy} maps are not effective in distinguishing the two families of patterns. ε_{yy} proves to be a better choice for differentiating the compressive patterns from the tensile patterns.

This stems from the fact that the remnant high angle bands have a tensile strain content and appear in red color on the ε_{yy} strain maps, whereas the newly forming $\pm 45^{\circ}$ bands have a compressive strain content and appear in blue color. Notice that at point u (Figure 4.36u) only the high angle bands are present (ignoring the very weak blue traces of the incipient $\pm 45^{\circ}$ on the lower left side of the sample). The blue bands (compressive patterns) form at point v, and several more blue bands form at point w (Figs. 4.36v and 4.36w respectively).

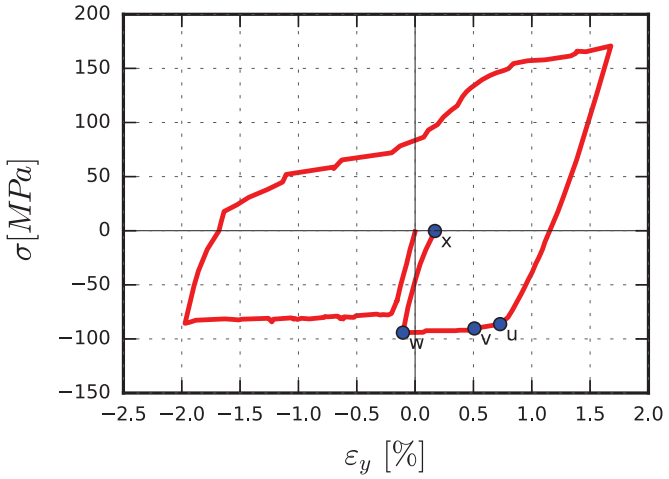

Figure 4.34. Micro-DIC analysis points u, v, and w are on the TP2 region, load point x is the last load point of the experiment.

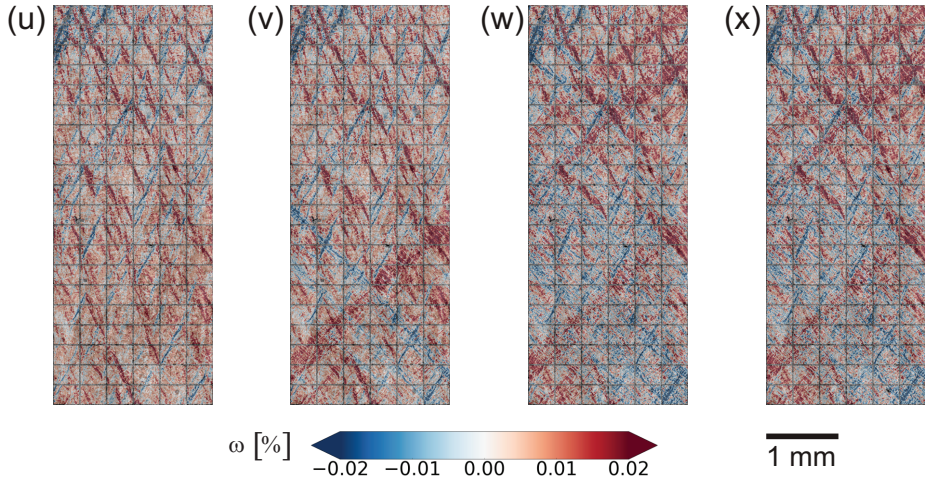

Figure 4.35. The ω_{xy} combination plots obtained for points u to x.

The $\pm 45^{\circ}$ TP2 bands differ from the TP1 bands in terms of distribution over the gage section.

Although the $\{10\bar{1}2\}\langle\bar{1}011\rangle$ twinning is the mechanism that drives the formation of both patterns, the TP2 patterns include the activation of many $\pm 45^{\circ}$ bands distributed across the sample surface whereas the TP1 patterns included the growth of 1-2 major bands to accommodate the imposed strain. The presence of the high angle bands in the material in TP2 apparently inhibits the formation of large 45° bands. The fact that the TP2 45° bands prefer to nucleate and expand at regions where high angle bands are less frequent supports this idea. Particularly, TP2 45° bands avoided the top side of the surface, whereas in the TP1 region a second major $+45^{\circ}$ band was formed on the top side of the surface. In further stages of the TP2 region, however, the two pattern families inevitably intertwine to accommodate additional compressive strain increments.

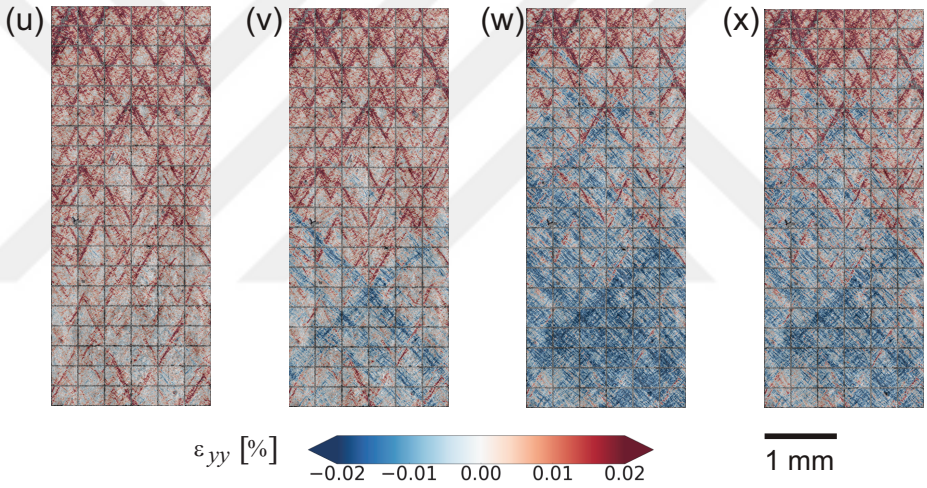

Figure 4.36. The ε_{yy} combination plots obtained for points u to x.

ε_{yy} maps and histograms of the frames (6,4), (5,4) and (3,4) are provided in Figure 4.37 to compare the level of strain heterogeneity before (point v) and after (point w) the formation of the TP2 bands. ε_{yy} is chosen over ω_{xy} in this section for the aforementioned reason of distinguishing the high angle bands and the $\pm 45^{\circ}$ TP2 bands by the sign of their strain content. The regions of all of selected frames accommodate some tensile strain content in the form of high angle bands (red colored patterns) at point v. As further compressive strain increments are imposed, $\pm 45^{\circ}$ patterns (blue) appear in each frame. Correspondingly, the strain histograms broaden towards the compressive strain side (from blue curves to green curves in Figure 4.37) at point w, most clearly observed for grid (5,4).

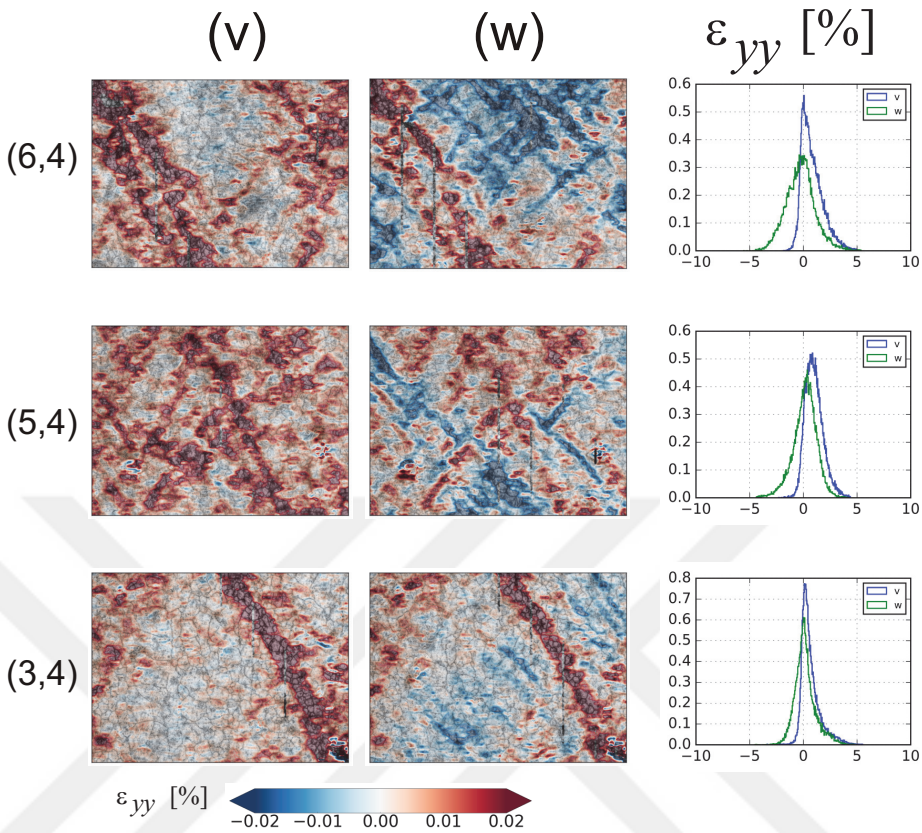

Figure 4.37. The ε_{yy} maps and histograms for the selected frames obtained for points v and w.

For this frame, the right side of the ε_{yy} histogram, representing the strain content of the high angle band structures, preserves its shape after the arrival of the $\pm 45^{\circ}$ bands. The broadening of the histograms is mainly due to spreading of the dormant populations (0 strain material points) towards the compressive side. This means that the originally dormant points are absorbed by the $\pm 45^{\circ}$ bands that bring about intense compressive strain at point w.

The resulting histograms (green curves) reveal the level of strain heterogeneity. Even though the frame averages of ε_{yy} are approximately 0 at point w, the deformation field consists of two different parts: Half of the region is under compression and the other half is under tension. The base ranges of the strain histograms are around 10% revealing acute strain heterogeneity. Note point w with $\varepsilon_M = -0.1\%$ and point l with $\varepsilon_M = 0.078\%$ are approximate crossing points of the zero strain axis.

The deformation fields measured at the macro- and micro-scales at the second crossing, point w (Figs. 4.35w and 4.37w respectively) are completely different from those of the first crossing point l (Figs. 4.13l and 4.15). Simply put, the first crossing revealed zero strain with near zero spread. In the second crossing, zero strain is only the average of very highly strained fields.

4.2.7. Effective Poisson's ratio

In the discussion that considered $\pm 45^{\circ}$ shear bands in the twin plateau, it was clarified that these are 2-D extruded structures that spanned through the thickness. The primary evidence was shown in Figure 4.8a revealing horizontal ε_{yy} bands on the side surface, with $\varepsilon_{zz} = 0$ and $\omega_{xy} = 0$ (Figure 4.8b). The microscopic connection of this macroscopic band was that the plane of shear of the two maximum-resolved-shear $\{10\bar{1}2\}\langle\bar{1}011\rangle$ twin variants inside the abundant orientation matches the macroscopic shear pattern. In addition to the evidence in literature, this also confirms that the strain localization stems from and is shaped by the tensile twin mechanism.

For further explanation of this point, effective Poisson's ratios on both top and side surface of the sample are calculated from the macroscale DIC data as:

$$\nu_{TD} = \frac{\varepsilon_{xx}}{\varepsilon_{yy}} \qquad\qquad \nu_{ND} = \frac{\varepsilon_{zz}}{\varepsilon_{yy}} \tag{4.2}$$

The calculated effective Poisson's ratios for both surfaces is plotted in Figure 4.38 against the load point number.

According to Figure 4.38, both ν_{TD} and ν_{ND} curves begin around 0.2-0.3, close to the expected value of Poisson's ratio in the elastic region. As soon as the sample undergoes yielding, ν_{TD} rapidly increases towards 1 and ν_{ND} approaches to 0. The measured Poisson's ratio means $\varepsilon_{yy} = -\varepsilon_{xx}$ on the TD surface and $\varepsilon_{zz} = 0$.

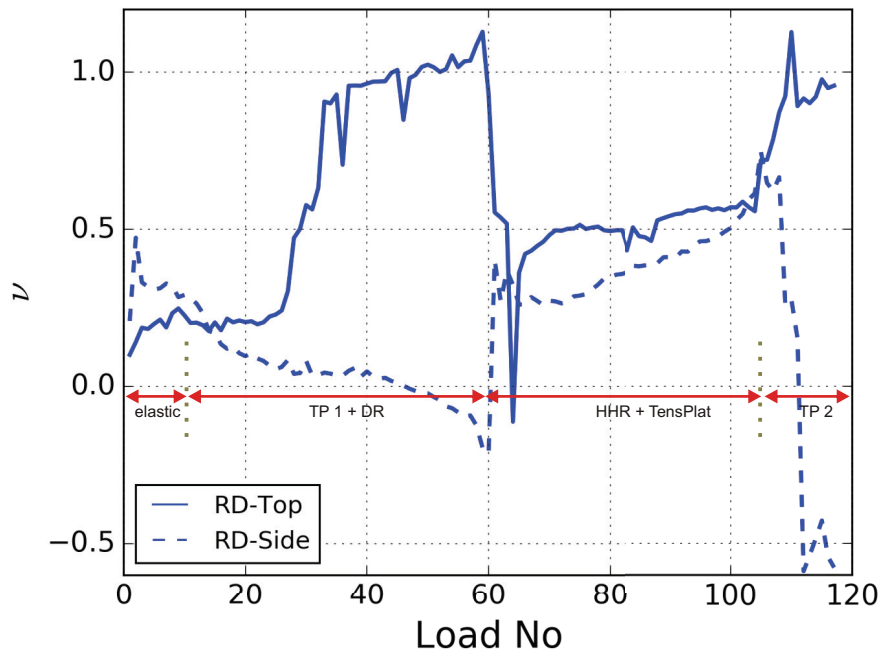

Figure 4.38. Effective Poisson's ratio computed from the macro-DIC data for the top and side surfaces.

This directly confirms our conclusion that $\pm 45^{\circ}$ volumetric shear bands observed in this stage are products of simple shear processes [34]. 2-D deformation patterns endure until the end of the detwinning ramp (DR) since the detwinning process is merely the reverse operation of the twin mechanism. In the HHR and TensPlat stages, on the other hand, ν curves both approach to 0.5% level, which is the common case for isotropic plastic (volume-preserving) behavior. Thus, the observed high angle band patterns in these stages are not products of simple shear processes whose plane of shear is exclusively confined to TD (pattern of TP1 bands). The results suggest 3-D activity of randomly-oriented shear processes (isotropy). As TP2 is reached, ν_{TD} curves, again, approach towards 1 signifying the formation of the new 2-D deformation structures in the TP2 stage. The side surface macro-DIC data in the TP2 stage reveals negative Poisson's ratio, a very curious result. The ν_{ND} value calculated for this stage is not yet deemed reliable.

4.2.8. Discussion

4.2.8.1. High angle bands. Although the strain localization around the high angle band structures in the HHR and TensPlat regions is not mechanistically understood so far, some general aspects of the deformation behavior in these regions are extensively presented in the previous sections. The high hardening rate in the TensPlat region (compared to TP1 and TP2), the homogeneous distribution of the high angle bands over the entire sample surface, and the isotropic behavior substantiated by the effective Poisson's ratio measurement in HHR and TensPlat point to domination of the dislocation slip. The literature survey detailed in Section 4.2.3 corroborates this conclusion. However, the deviation of the band orientations from the maximum shear planes necessitates a specific micro-mechanistic explanation.

A microscale aspect of individual high angle bands is shown in Figure 4.39 that provides ω_{xy} maps for selected regions of interest. Each high angle band structure forms and develops over grain clusters with consistently small grain sizes. The bands tend to avoid the large grains around these clusters. Strain localization around small grains can be explained with the high stress gradients which can facilitate activation of harder deformation mechanisms. Abundance of grain boundary area over clusters of small grains is a well-known factor that can foster localization over them due to geometrically necessary dislocation density [39, 51, 52]. However, preference of small grain clusters does not appear to be a standalone governing factor since that cannot explain the structured orientations of these bands. Rather, possibly the small grains tend to have higher volume fraction of remnant twin bands that do not completely detwin at the end of DR. One connected explanation that attempts to account for the observed angle of the high angle bands, is the activity of type II $\langle c + a \rangle$ pyramidal slip system over remnant twin orientations (c-axis roughly aligned with the load).

Such deformation yields about 60° inclination from horizontal which is consistent with the observed patterns. The collective long-range stress field of the dislocation clusters in such a case could produce the observed side surface patterns. This conclusion, however, is not substantiated with any direct physical evidence yet.

The $\{10\bar{1}1\}\langle 10\bar{1}\bar{2}\rangle$ mechanism might also be proposed since twinning mechanisms show a tendency to localize strain patterns due to the local stress concentration twin bands impose in its locality. However, the operation angle of the compressive twin is about 27° from the horizontal for the initial orientations (c-axis normal to the load) whereas for any tensile twin remnants (c-axis aligned with the load) the compressive twin wouldn't operate under tension. A decisive conclusion about the nature of the high angle bands requires further experimental investigation.

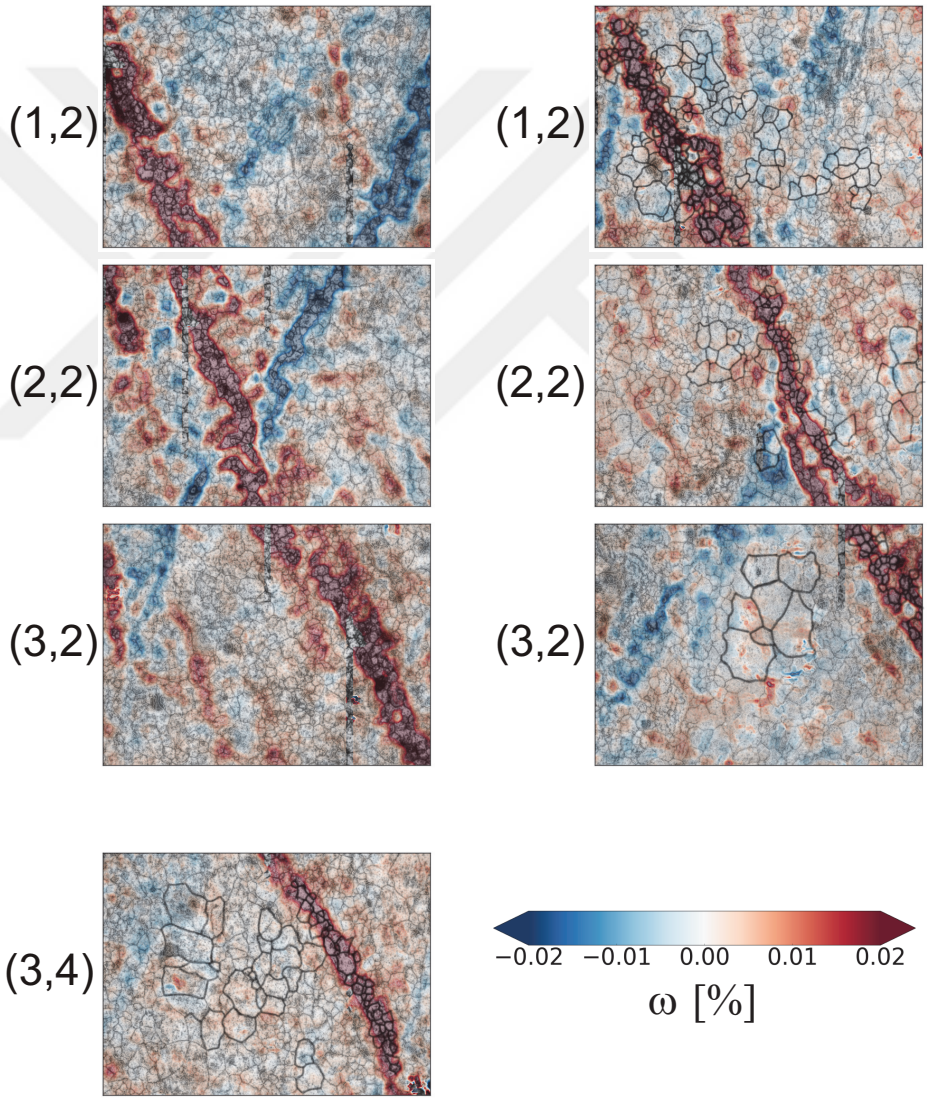

Figure 4.39. The high angle shear band path microstructure characterized with smaller grain size compared to rest of the material.

5. CONCLUSION

A tension-compression sample cut from a rolled Mg AZ31 hot-rolled plate is loaded along its rolling direction (RD) in compression-tension-compression. In the course of this 1,5 cycle loading experiment, two orthogonal faces of the sample, that coincide with the in-plane transverse direction (TD) and plate normal (ND) are monitored *in-situ* with optical imaging. The TD surface is observed with microscale and macroscale optical systems, whereas the ND surface is observed only with macroscale optics. Microscopic observation of the TD surface involves scanning the entire face with a high sensitivity positioning system to achieve full-field examination. Full-field deformation maps are measured with digital image correlation at every load step, monitoring the evolution of deformation patterns. The heterogeneous deformation characteristics are investigated to help develop an understanding of the mechanical behavior in terms of operational micromechanisms and the crystallographic texture.

The sample deformation in the first compression stage of the experiment is dominated by the tensile twin mechanism for this texture. In this stage, $\pm 45^{\circ}$ shear band patterns form at both the macroscale and microscale. With the help of in-plane rotation maps and the conclusions of the Aydıner and Telemez (2014) [34] study, the $\pm 45^{\circ}$ bands are identified as products of simple shear processes at multiple length scales. This includes the macroscopic (sample) length scale, i.e., the sample accommodates imposed strain by macroscopic shear banding. The $\pm 45^{\circ}$ bands at the microscale are directly related to twinning processes. The $\pm 45^{\circ}$ shear bands at the microscale coordinate to form the macroscale $\pm 45^{\circ}$ shear band patterns. At both length scales, shear bands cause high deformation heterogeneity characterized by broadened histograms with multiple strain populations.

As the material is loaded in the reverse direction right after the compression stage, the tensile strain increments are accommodated effectively by the detwinning process. All deformation activity in this stage takes place inside the preexisting shear bands, leaving the rest of the material dormant.

Preexisting $\pm 45^{\circ}$ shear bands shrink and the deformation is effectively reversed. Detwinning that gets activated at very low tensile stress levels, leads to the untypical sigmoidal shape of the stress-strain curve.

The third stage of deformation comprised of the high-hardening ramp and tensile plateau regions, that roughly starts when the sample switches over to positive strain. Here, strain heterogeneity appeared in the form of high angle shear localization bands that are mesoscale structures, not resolved with macroscopic DIC. Though these bands occupy smaller regions compared to the $\pm 45^{\circ}$ bands, their strain intensity is higher. Further, very curiously, these bands deviate from the maximum shear planes, by approximately 15°. Though the detection of these interesting structures was the most important experimental novelty of this study, a mechanistic understanding of their origin is yet to be acquired. Future work regarding this effort is described in the next chapter.

The sample is then unloaded from the tensile stress/strain state and reverse-loaded into compression. A nearly perfectly-plastic plateau starts at a stress level approximately 10% higher than the stress level of the initial twin plateau as the last segment of the experiment. $\pm 45^{\circ}$ shear bands associated with coordinated tensile twin activity once again is the predominant mode of strain accommodation. However, the morphology of the bands is different in this stage, mainly due to the residual plasticity remained from the high angle shear bands of the previous stage. The$\pm 45^{\circ}$ bands appear at a higher frequency, and consistently, their individual regions of activity are smaller.

Macroscopic observation of the side (ND) surface enabled deduction of volumetric information about the tensile-twin associated shear bands. Traces of these bands are discerned as horizontal streaks on the side surface ε_{yy} maps. The overall geometry of these bands can be deduced from the $\pm 45^{\circ}$ orientation on the TD surface and the horizontal trace on the ND surface: These are $\pm 45^{\circ}$ bands whose plane of shear is exclusively confined to the TD plane; they are volumetric and are extruded 2-D structures that run through thickness of the sample. This is consistent with the findings of Aydıner and Telemez [34]. In the detwinning stage, band recovery is observed on the side surface simultaneously with the top surface.

Hence, we conclude that strain recovery in the DR stage is also volumetric.

The behaviour on HHR and Tensile Plateau are more compound compared to the twin plateau and DR behaviors. A horizontal streak on the side surface was visible in the tensile plateau. The effective Poisson's ratio for both surfaces was measured using macroscopic DIC data. The effective Poisson's ratio on the TD surface is close to one in the twin plateau and detwinning ramp, and is close to zero on the ND surface. This is consistent with the aforementioned 2-D simple shear pattern in these stages. However, a mechanism change is apparent at the boundary of the DR and HHR stages, where the effective Poisson's ratio curves move towards a value of 0.5, indicating an isotropic plastic behavior. The effective Poisson's ratio curves are consistent with the presumed behavior for the twin plateau and detwinning ramp stages. However, further analysis is needed to reconcile the deformation maps and measured Poisson's ratio curves for the HHR and tensile plateau regions.

At the microscale, the high angle shear bands are observed follow small-grain clusters and avoid large grains. When loaded along a *hard orientation*, the associated hard mechanisms are more likely to be activated in a small grained region with stress concentration sites. However, this does not provide a satisfactory explanation of the systematic high angle activation of the shear processes at this stage. The mechanism behind the observed high angle bands is yet to be determined.

In all steps of deformation, representative volume element concept (RVE) is either not applicable or barely applicable. In the twin plateau, the band structures are sample size, that implies there is no acceptable size for an RVE. In HHR, the deformation is more homogeneous and the localization, though still large (1 mm typical size), largely disappears from the detection of macroscopic DIC. Nevertheless, the deformation exhibits high heterogeneity at every stage, partially remnant from the end of the first twin plateau. Each stage displays characteristic structured deformation heterogeneity. Material models should incorporate more accurate physical models to account for the observed behavior.

6. FUTURE WORK

The mechanism responsible for the formation of the high angle bands is yet to be identified. The effect of prior deformation on the formation of these high angle bands is an another research topic. To target the first issue, new compression-tension along RD experiments will be conducted. Texture measurement with X-Ray diffraction will be performed at the fully unloaded state after a compression-tension cycle (point s in the present study). Texture measurement at this load point will reveal the unrecovered part of the material as a residual peak at the periphery of the $\{0001\}$ pole figure (see Figure 2.2). Furthermore, texture measurement at that point will pinpoint the micromechanism that leads to the formation of high angle bands by revealing the distinctive texture evolution that accompanies the collective activity of the mechanism.

Apart from the texture measurement study cited above, direct tension experiments will be performed on the identical samples and the results will be compared to the present ones to investigate the effect of prior compressive loading on the tensile plasticity of the sample. The clear aim here is to track formation of any similar structures to the high angle bands.

REFERENCES

1. Christian, J. and S. Mahajan, "Deformation twinning", *Progress in Materials Science*, Vol. 39, No. 1, pp. 1 – 157, 1995.

2. Yoo, M. and J. Lee, "Deformation twinning in hcp metals and alloys", *Philosophical Magazine A*, Vol. 63, No. 5, pp. 987–1000, 1991.

3. Hosford, W. F., *Mechanical Behavior of Materials*, Cambridge University Press, Cambridge, UK, 2. edition, 2010.

4. Brown, D., S. Agnew, M. Bourke, T. Holden, S. Vogel, and C. Tomé, "Internal strain and texture evolution during deformation twinning in magnesium", *Materials Science and Engineering: A*, Vol. 399, No. 1, pp. 1–12, 2005.

5. Lou, X., M. Li, R. Boger, S. Agnew, and R. Wagoner, "Hardening evolution of AZ31B Mg sheet", *International Journal of Plasticity*, Vol. 23, No. 1, pp. 44–86, 2007.

6. Koike, J., "Enhanced deformation mechanisms by anisotropic plasticity in polycrystalline Mg alloys at room temperature", *Metallurgical and Materials Transactions A*, Vol. 36, No. 7, pp. 1689–1696, 2005.

7. Aydıner, C., J. Bernier, B. Clausen, U. Lienert, C. Tomé, and D. Brown, "Evolution of stress in individual grains and twins in a magnesium alloy aggregate", *Physical Review B*, Vol. 80, No. 2, p. 024113, 2009.

8. Mohr, D., M.-A. Chevin, and L. Greve, "Deformation Behavior of Magnesium Extrusions With Strong Basal Texture: Experiments and Modeling", *Journal of Applied Mechanics*, Vol. 80, No. 6, p. 061002, 2013.

9. Wang, Y. and J. Huang, "The role of twinning and untwinning in yielding behavior in hot-extruded Mg–Al–Zn alloy", *Acta Materialia*, Vol. 55, No. 3, pp. 897–905, 2007.

10. Knezevic, M., A. Levinson, R. Harris, R. K. Mishra, R. D. Doherty, and S. R. Kalidindi, "Deformation twinning in AZ31: influence on strain hardening and texture evolution", *Acta Materialia*, Vol. 58, No. 19, pp. 6230–6242, 2010.

11. Clausen, B., C. Tomé, D. Brown, and S. Agnew, "Reorientation and stress relaxation due to twinning: modeling and experimental characterization for Mg", *Acta Materialia*, Vol. 56, No. 11, pp. 2456–2468, 2008.

12. Abdolvand, H., M. Majkut, J. Oddershede, S. Schmidt, U. Lienert, B. J. Diak, P. J. Withers, and M. R. Daymond, "On the deformation twinning of Mg AZ31B: A three-dimensional synchrotron X-ray diffraction experiment and crystal plasticity finite element model", *International Journal of Plasticity*, Vol. 70, pp. 77–97, 2015.

13. Abdolvand, H. and M. R. Daymond, "Internal strain and texture development during twinning: comparing neutron diffraction measurements with crystal plasticity finite-element approaches", *Acta Materialia*, Vol. 60, No. 5, pp. 2240–2248, 2012.

14. Wang, F., S. Sandlöbes, M. Diehl, L. Sharma, F. Roters, and D. Raabe, "In situ observation of collective grain-scale mechanics in Mg and Mg–rare earth alloys", *Acta Materialia*, Vol. 80, pp. 77–93, 2014.

15. Beyerlein, I., L. Capolungo, P. Marshall, R. McCabe, and C. Tomé, "Statistical analyses of deformation twinning in magnesium", *Philosophical Magazine*, Vol. 90, No. 16, pp. 2161–2190, 2010.

16. Jain, A., O. Duygulu, D. Brown, C. Tomé, and S. Agnew, "Grain size effects on the tensile properties and deformation mechanisms of a magnesium alloy, AZ31B, sheet", *Materials Science and Engineering: A*, Vol. 486, No. 1, pp. 545–555, 2008.

17. Gu, C., L. Toth, and M. Hoffman, "Twinning effects in a polycrystalline magnesium alloy under cyclic deformation", *Acta Materialia*, Vol. 62, pp. 212–224, 2014.

18. Proust, G., C. N. Tomé, A. Jain, and S. R. Agnew, "Modeling the effect of twinning

and detwinning during strain-path changes of magnesium alloy AZ31", *International Journal of Plasticity*, Vol. 25, No. 5, pp. 861–880, 2009.

19. Wu, W., P. K. Liaw, and K. An, "Unraveling cyclic deformation mechanisms of a rolled magnesium alloy using in situ neutron diffraction", *Acta Materialia*, Vol. 85, pp. 343–353, 2015.

20. Wu, L., A. Jain, D. Brown, G. Stoica, S. Agnew, B. Clausen, D. Fielden, and P. Liaw, "Twinning–detwinning behavior during the strain-controlled low-cycle fatigue testing of a wrought magnesium alloy, ZK60A", *Acta Materialia*, Vol. 56, No. 4, pp. 688–695, 2008.

21. Wu, L., S. Agnew, D. Brown, G. Stoica, B. Clausen, A. Jain, D. Fielden, and P. Liaw, "Internal stress relaxation and load redistribution during the twinning–detwinning-dominated cyclic deformation of a wrought magnesium alloy, ZK60A", *Acta Materialia*, Vol. 56, No. 14, pp. 3699–3707, 2008.

22. Hama, T., N. Kitamura, and H. Takuda, "Effect of twinning and detwinning on inelastic behavior during unloading in a magnesium alloy sheet", *Materials Science and Engineering: A*, Vol. 583, pp. 232–241, 2013.

23. Lee, S., H. Wang, M. Gharghouri, G. Nayyeri, W. Woo, E. Shin, P. Wu, W. Poole, W. Wu, and K. An, "Deformation behavior of solid-solution-strengthened Mg–9 wt.% Al alloy: In situ neutron diffraction and elastic–viscoplastic self-consistent modeling", *Acta Materialia*, Vol. 73, pp. 139–148, 2014.

24. Zhang, J., Q. Yu, Y. Jiang, and Q. Li, "An experimental study of cyclic deformation of extruded AZ61A magnesium alloy", *International Journal of Plasticity*, Vol. 27, No. 5, pp. 768–787, 2011.

25. Yu, Q., J. Zhang, and Y. Jiang, "Fatigue damage development in pure polycrystalline magnesium under cyclic tension–compression loading", *Materials Science and Engi-*

neering: A, Vol. 528, No. 25, pp. 7816–7826, 2011.

26. Guillemer, C., M. Clavel, and G. Cailletaud, "Cyclic behavior of extruded magnesium: Experimental, microstructural and numerical approach", *International Journal of Plasticity*, Vol. 27, No. 12, pp. 2068–2084, 2011.

27. Huppmann, M., M. Lentz, S. Chedid, and W. Reimers, "Analyses of deformation twinning in the extruded magnesium alloy AZ31 after compressive and cyclic loading", *Journal of Materials Science*, Vol. 46, No. 4, pp. 938–950, 2011.

28. Caceres, C., T. Sumitomo, and M. Veidt, "Pseudoelastic behaviour of cast magnesium AZ91 alloy under cyclic loading–unloading", *Acta Materialia*, Vol. 51, No. 20, pp. 6211–6218, 2003.

29. Mann, G., T. Sumitomo, C. Caceres, and J. Griffiths, "Reversible plastic strain during cyclic loading–unloading of Mg and Mg–Zn alloys", *Materials Science and Engineering: A*, Vol. 456, No. 1, pp. 138–146, 2007.

30. Muránsky, O., D. Carr, P. Šittner, and E. Oliver, "In situ neutron diffraction investigation of deformation twinning and pseudoelastic-like behaviour of extruded AZ31 magnesium alloy", *International Journal of Plasticity*, Vol. 25, No. 6, pp. 1107–1127, 2009.

31. Lee, S. and M. Gharghouri, "Pseudoelastic behavior of magnesium alloy during twinning-dominated cyclic deformation", *Materials Science and Engineering: A*, Vol. 572, pp. 98–102, 2013.

32. Wu, L., S. Agnew, Y. Ren, D. Brown, B. Clausen, G. Stoica, H. Wenk, and P. Liaw, "The effects of texture and extension twinning on the low-cycle fatigue behavior of a rolled magnesium alloy, AZ31B", *Materials Science and Engineering: A*, Vol. 527, No. 26, pp. 7057–7067, 2010.

33. Wang, H., P. Wu, C. Tomé, and J. Wang, "A constitutive model of twinning and detwinning for hexagonal close packed polycrystals", *Materials Science and Engineering: A*,

Vol. 555, pp. 93–98, 2012.

34. Aydıner, C. C. and M. A. Telemez, "Multiscale deformation heterogeneity in twinning magnesium investigated with in situ image correlation", *International Journal of Plasticity*, Vol. 56, pp. 203–218, 2014.

35. Carroll, J., W. Abuzaid, J. Lambros, and H. Sehitoglu, "An experimental methodology to relate local strain to microstructural texture", *Review of Scientific Instruments*, Vol. 81, No. 8, p. 083703, 2010.

36. Hazeli, K., A. Sadeghi, M. Pekguleryuz, and A. Kontsos, "The effect of strontium in plasticity of magnesium alloys", *Materials Science and Engineering: A*, Vol. 578, pp. 383–393, 2013.

37. Murasawa, G., R. Takahashi, T. Morimoto, and S. Yoneyama, "Inhomogeneous deformation twinning measurement using digital image correlation and acoustic emission", *Experimental Mechanics*, Vol. 55, No. 1, pp. 65–76, 2015.

38. Efstathiou, C. and H. Sehitoglu, "Strain hardening and heterogeneous deformation during twinning in Hadfield steel", *Acta Materialia*, Vol. 58, No. 5, pp. 1479–1488, 2010.

39. Efstathiou, C., H. Sehitoglu, and J. Lambros, "Multiscale strain measurements of plastically deforming polycrystalline titanium: role of deformation heterogeneities", *International Journal of Plasticity*, Vol. 26, No. 1, pp. 93–106, 2010.

40. Padilla, H., J. Lambros, A. Beaudoin, and I. Robertson, "Relating inhomogeneous deformation to local texture in zirconium through grain-scale digital image correlation strain mapping experiments", *International Journal of Solids and Structures*, Vol. 49, No. 1, pp. 18–31, 2012.

41. Eskandari, M., M. Yadegari-Dehnavi, A. Zarei-Hanzaki, M. Mohtadi-Bonab, R. Basu, and J. Szpunar, "In-situ strain localization analysis in low density transformation-twinning induced plasticity steel using digital image correlation", *Optics and Lasers*

in Engineering, Vol. 67, pp. 1–16, 2015.

42. Britton, T., F. Dunne, and A. Wilkinson, "On the mechanistic basis of deformation at the microscale in hexagonal close-packed metals", *Proc. R. Soc. A*, Vol. 471, No. 2178, p. 20140881, 2015.

43. Kim, D.-H., M. Manuel, F. Ebrahimi, J. Tulenko, and S. Phillpot, "Deformation processes in-textured nanocrystalline Mg by molecular dynamics simulation", *Acta Materialia*, Vol. 58, No. 19, pp. 6217–6229, 2010.

44. Guo, Y.-F., S. Xu, X.-Z. Tang, Y.-S. Wang, and S. Yip, "Twinnability of HCP Metals at the Nanoscale", *Journal of Applied Physics*, Vol. 115, No. 22, p. 224902, 2014.

45. Suwas, S. and R. K. Ray, *Crystallographic Texture of Materials*, Springer, London, 2014.

46. Wang, Y. and J. Huang, "Texture analysis in hexagonal materials", *Materials Chemistry and Physics*, Vol. 81, No. 1, pp. 11–26, 2003.

47. Geusebroek, J.-M., F. Cornelissen, A. W. Smeulders, and H. Geerts, "Robust autofocusing in microscopy", *Cytometry*, Vol. 39, No. 1, pp. 1–9, 2000.

48. Sutton, M. A., J. J. Orteu, and H. Schreier, *Image correlation for shape, motion and deformation measurements: basic concepts, theory and applications*, Springer Science & Business Media, New York, NY, USA, 2009.

49. Vendroux, G. and W. Knauss, "Submicron deformation field measurements: Part 2. Improved digital image correlation", *Experimental Mechanics*, Vol. 38, No. 2, pp. 86–92, 1998.

50. Chu, T., W. Ranson, and M. Sutton, "Applications of digital-image-correlation techniques to experimental mechanics", *Experimental Mechanics*, Vol. 25, No. 3, pp. 232–244, 1985.

51. Sachtleber, M., Z. Zhao, and D. Raabe, “Experimental investigation of plastic grain interaction”, *Materials Science and Engineering: A*, Vol. 336, No. 1, pp. 81–87, 2002.

52. Dunne, F., R. Kiwanuka, and A. Wilkinson, “Crystal plasticity analysis of micro-deformation, lattice rotation and geometrically necessary dislocation density”, *Proc. R. Soc. A*, Vol. 468, No. 2145, pp. 2509–2531, 2012.